Advanced Materials

ADVANCED MATERIALS
www.advmat.de

RESEARCH ARTICLE

Biodegradable Self-Enhancing Piezoelectric Scaffold for Synchronized Tendon-to-Bone Regeneration

Longfei Li[1,2,3] | Dengjie Yu[1,4,5] | Jiaxuan Li[1,2] | Ruizeng Luo[1,3,6] | Xi Cui[1,3,6] | Yadong Zhang[5] | Yusheng Li[7,8] | Yantao Zhao[5,9] | Zhou Li[3,6]

[1]Beijing Institute of Nanoenergy and Nanosystems, Chinese Academy of Sciences, Beijing, P. R. China | [2]School of Nanoscience and Engineering, University of Chinese Academy of Sciences, Beijing, P. R. China | [3]Vita Tech Innovation Center, Beijing Tsinghua Changgung Hospital, School of Clinical Medicine, Tsinghua University, Beijing, P. R. China | [4]Medical School of Chinese PLA, Beijing, P. R. China | [5]Department of Orthopedics, the Fourth Medical Center of PLA General Hospital, Beijing, P. R. China | [6]School of Biomedical Engineering, Tsinghua Medicine, Tsinghua University, Beijing, P. R. China | [7]Department of Orthopedics, Xiangya Hospital, Central South University, Changsha, P. R. China | [8]National Clinical Research Center for Geriatric Disorders, Xiangya Hospital, Central South University, Changsha, P. R. China | [9]Beijing Engineering Research Center of Orthopedics Implants, Beijing, P. R. China

Correspondence: Yusheng Li (liyusheng@csu.edu.cn) | Yantao Zhao (biodoctor1981@163.com) | Zhou Li (li_zhou@tsinghua.edu.cn)

Received: 16 January 2026 | **Revised:** 24 May 2026 | **Accepted:** 2 July 2026

Keywords: biomedical engineering | electrical stimulation | piezoelectric scaffold | rotator cuff repair | tendon–bone interface

ABSTRACT

A key challenge in contemporary rotator cuff repair lies in achieving spatiotemporally specific differentiation of stem cells within the intricate tendon–bone interface (TBI) microenvironment, thereby enabling the synchronous regeneration of functionally graded tendon, fibrocartilage, and bone tissues. Existing scaffold designs often fail to adequately replicate the mechanical gradients and biochemical heterogeneity of the natural TBI microenvironment, particularly in reconstructing the precise spatial organization of the tendon–cartilage–bone transitional zone. This study innovatively integrates the in situ electrical stimulation advantages of piezoelectric degradable scaffolds, the topological guidance mediated by electrospun fibers, and biomimetic mineralization capabilities to construct a "mechanical–electrical–biochemical cue" coupled system for structural reconstruction and functional restoration of TBI. The gradient scaffold, designed with structural-component matching, generates a piezoelectric enhancement effect during stress concentration, creating precise electrical stimulation and mechanical microenvironment gradients within the fiber scaffold. This enhanced electrical signal is three times greater than the piezoelectric performance of traditional poly(L-lactic acid) scaffolds. This dynamically controllable electrical signal activates the PI3K/AKT signaling pathway, modulating mesenchymal stem cells differentiation toward tenogenic, chondrogenic, and osteogenic lineages. In a rat rotator cuff tear (RCT) model, this gradient-structured, fully biodegradable scaffold combined with electrical stimulation therapy was demonstrated to achieve coordinated multi-tissue regeneration in complex TBI.

1 | Introduction

The shoulder joint, the most mobile joint, relies heavily on the rotator cuff to maintain dynamic stability and enable multidirectional mobility [1]. Due to acute or chronic factors such as aging, trauma, and repetitive overuse, rotator cuff injuries are one of the most prevalent musculoskeletal disorders, affecting over 30% of patients and often resulting in chronic pain and joint mobility impairment [2, 3]. In clinical practice, surgical repair of the tendon–bone attachment is the primary treatment

Longfei Li and Dengjie Yu contributed equally to the work.

for rotator cuff tears (RCTs) [4]. However, this approach only restores the anatomical continuity of the rotator cuff and fails to reconstruct the biological integrity of the tendon–bone interface (TBI) [5]. Moreover, the regenerated tissue mainly comprises mechanically inferior fibrous scar tissue, resulting in a high postoperative re-tear rate ranging from 20% to 94% [6, 7]. The most critical barrier in rotator cuff repair is the inability to regenerate the native multiscale gradient and microenvironment of the TBI. The native TBI is a complex hierarchical interface characterized by a four-layered structure consisting of tendon, non-calcified fibrocartilage, calcified fibrocartilage, and bone [8, 9]. Mechanically, this hierarchical organization minimizes stress concentration and enables effective load transfer between tendon and bone [10, 11]. Biologically, resident cell populations maintain local homeostasis by secreting specific extracellular matrix proteins [12, 13].

Scaffold-based tissue engineering has become a promising strategy to facilitate the regeneration of the TBI and promote functional recovery [14]. To achieve this, an ideal scaffold must recapitulate the native TBI by incorporating spatially graded variations in architecture, composition, and mechanical properties [13]. Accordingly, such a scaffold should be able to orchestrate multi-lineage differentiation, temporally and spatially guiding stem cells differentiation into tenocytes, chondrocytes, and osteocytes within discrete scaffold regions, thereby achieving synchronized regeneration [15]. Recent advancements in tissue engineering and interface regeneration technologies have yielded innovative solutions for TBI integration, encompassing 3D-printed hierarchical constructs [16], multilayer electrospun fiber scaffolds [17, 18], biomimetic mineralization [19], gradient modification of bioactive substances (e.g., growth factors, cells) [20, 21], composite hydrogel scaffolds [4, 22], and smart responsive systems [23]. However, scaffolds relying solely on architectural cues often fail to achieve the desired efficiency of cell differentiation, leading to suboptimal healing outcomes [24]. Biochemical factors can also accelerate tendon–bone healing by stimulating cell proliferation and differentiation [25]. However, the spatial variability in the distribution of biochemical factors required for multicellular interfaces during TBI remodeling limits their practical application, along with risks such as heterotopic ossification [26].

To address these challenges, electrical stimulation (ES) provided an innovative strategy for rotator cuff repair [27]. ES not only effectively restores the inherent electrophysiological microenvironment of rotator cuff tissue but also overcomes the immunogenicity risks and high-cost limitations associated with conventional biochemical therapies [5, 28]. Compared to traditional ES, an in situ ES system based on piezoelectric materials can generate endogenous dynamic electric fields under physiological mechanical loads or ultrasound (US) [29, 30], enabling non-invasive spatiotemporal dynamic regulation of physical signals while eliminating the risks of secondary surgery and infection [5, 31]. Notably, biodegradable piezoelectric biomaterials exhibit distinct therapeutic advantages for this interfacial tissue repair [32]. They transient electromechanical support adaptively modulates interfacial stress distribution while delivering endogenous electrical stimuli to guide cellular responses [33]. Furthermore, their controlled degradation allows for the progressive transfer of mechanical loads to newly formed tissue, thereby synchronizing with the tissue regeneration process [34, 35]. For example, poly(L-lactic acid) (PLLA), which combines piezoelectric and controllable degradability properties, has been demonstrated to promote the orderly alignment of collagen fibers in the tendon region [36], enhance the secretion of cartilage extracellular matrix [37, 38], and upregulate expression of osteogenesis-related genes [39].

Building upon these insights, we designed an innovative biodegradable piezoelectric bilayer fiber scaffold to achieve the synchronized regeneration of the TBI (Scheme 1). The aligned PLLA nanofibers replicate the natural tendon architecture, providing tendon-specific topographical cues and ES that facilitate tenocyte proliferation and alignment. Concurrently, random PLLA/hydroxyapatite (HAp) nanofibers act as calcium phosphate reservoirs to initiate biomineralization cascades and support bone formation. Notably, this dual architecture supports tissue-specific microenvironments and synergistically enhances piezoelectric output through stress concentration, effectively overcoming the insufficient piezoelectric response in conventional single-phase PLLA materials. Crucially, US-mediated piezoelectric stimulation generates electrical and mechanical microenvironment gradients within the scaffold, guiding mesenchymal stem cells (MSCs) to differentiate toward chondrocytes at the interfaces of gradient fibers. By employing this "topological scaffold-electrical stimulation" strategy, the scaffold not only provides specific biophysical signals but also converts external ES into cellular-level regulation via the piezoelectric effect, enabling spatiotemporal precise control of MSCs differentiation toward tenogenic, chondrogenic, and osteogenic lineages by activating the PI3K/AKT signaling pathway. In vivo, this piezoelectric scaffold effectively improved the rotator cuff's structural remodeling and functional recovery, indicating that this approach can facilitate the hierarchical complexity of TBI regeneration, which offers novel insights and therapeutic strategies for interface tissue engineering.

2 | Results

2.1 | Fabrication and Characterization of Bilayer Piezoelectric Nanofiber Scaffold

A dual-layer membrane was prepared via the sequence spinning technique, wherein the PLLA fiber membrane exhibits an oriented fiber structure while the PLLA/HAp layer retains a disordered structure (Figure 1A–C). Both fiber structures endow the features that mimic the biomechanical and topographical cues of the native extracellular matrix (ECM). The average diameter of PLLA fibers is 650 nm, while that of PLLA/HAp fibers is 950 nm. Moreover, due to the effective doping of HAp, the elemental mapping reveals well-defined Ca and P element distribution throughout the fibers (Figure S1). The new absorption peaks observed in the FTIR of PLLA/HAp are located in the 900–1200 cm^{-1} and 560–640 cm^{-1} regions, corresponding to the vibrations of phosphate and hydroxyl groups, respectively (Figure S2). To facilitate subsequent cell culture, the overall hydrophilicity of the fiber scaffold was significantly improved following treatment with a plasma cleaner (Figure S3). Figure 1D shows the cross-sectional morphology of the bilayer fiber membrane. It can be observed that the upper and lower layers exhibit distinct fiber

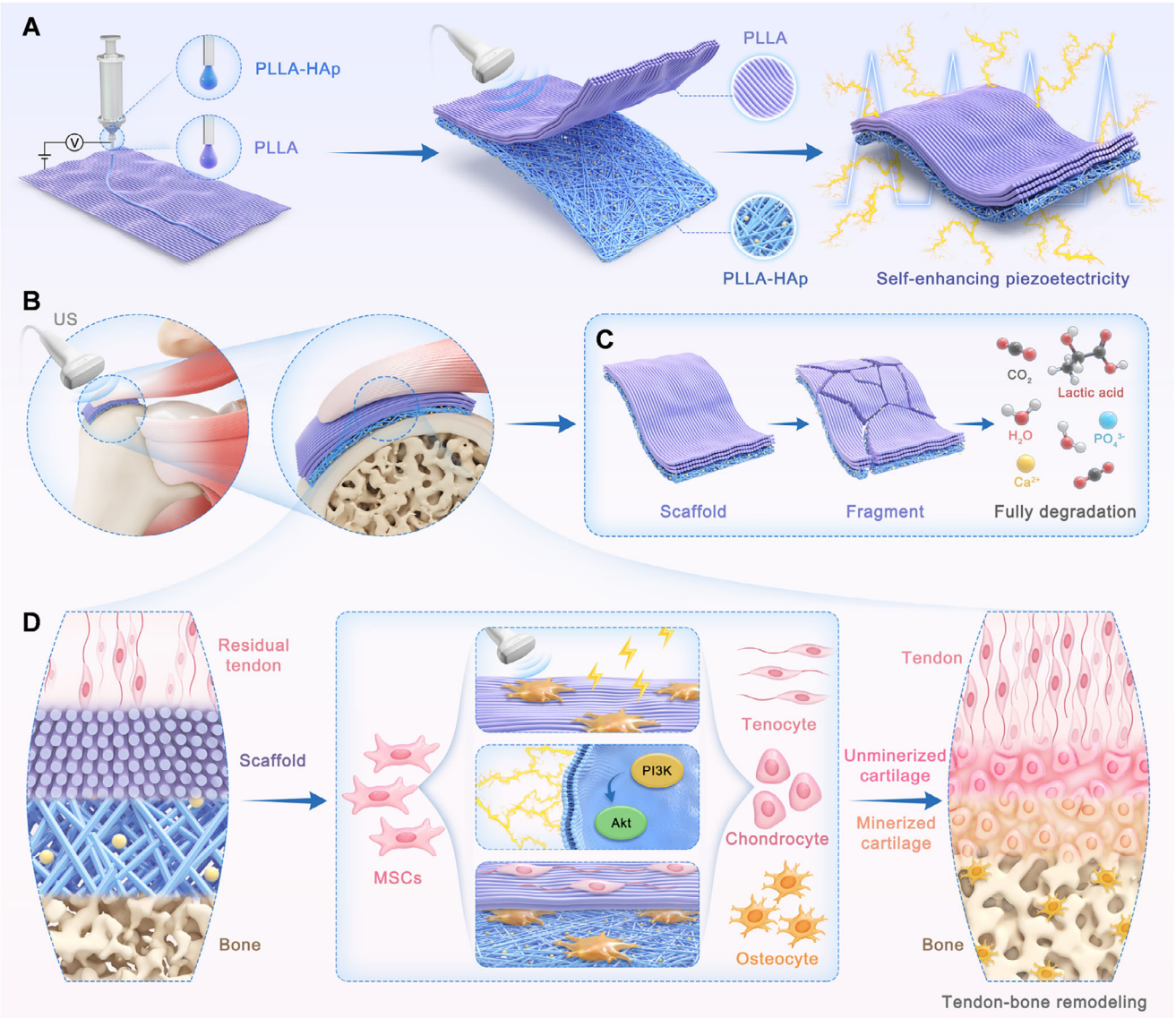

SCHEME 1 | A diagram of rotator cuff injury treatment based on the piezoelectric-driven biodegradable nanofiber scaffold. (A) Electrospun PLLA/PLLA-HAp bilayer piezoelectric fiber membrane with enhanced piezoelectric effect. (B) Schematic of piezoelectric fiber scaffold implantation into the rotator cuff and US-generated electrical stimulation. (C) Display of the scaffold's fully biodegradable properties. (D) Schematic diagram of the piezoelectric scaffold synchronous repair of tendon–cartilage–bone tissues.

orientation differences, with Ca and P elements appearing only in the upper layer (PLLA-HAp). Figure 1E further verifies the HAp content in the different fiber membranes. For PLLA nanofibers, the crystallinity of β-type crystals is a key factor in determining their piezoelectric properties [40, 41]. Compared to the unannealed PLLA fiber membrane (control group), the annealed PLLA and bilayer fiber scaffold (composite group) exhibited a peak at 16.5°, confirming the presence of (200) and (110) crystal planes corresponding to the β-phase structure (Figure 1F). The annealed PLLA-HAp fibers also demonstrated the existence of the β-phase, though with weaker peaks than those observed in the PLLA membrane (Figure S4). Mechanical property is also a crucial factor in evaluating the rotator cuff as a load-bearing structure. Compared to PLLA fibers, the bilayer fiber membrane exhibits greater tensile strain (113%) and slightly lower tensile strength (20.95 MPa) (Figures 1G and S5). This can be attributed to the random PLLA/HAp coating on the aligned PLLA fibers, which weakens mechanical strength along the orientation direction but enhances flexibility.

2.2 | Piezoelectric Properties and Self-Enhancing Piezoelectric Mechanism

Compared to the control group, the annealed PLLA fiber membrane exhibited outputs of ≈0.95 V, 6.16 nA, and 0.52 nC (Figures 2A and S6). The composite scaffold displays a more optimal output of ≈2.85 V, 17.46 nA, and 1.42 nC at the same thickness and size (normalized according to the thickness shown in Figure S7), about three times that of the PLLA fibers alone. Additionally, Figure 2B illustrates the piezoelectric output generated by applying ultrasonic waves with an intensity of 2 W/cm^2 and a frequency of 1 MHz through the US. The composite scaffold also exhibits higher output than the PLLA fiber scaffold alone,

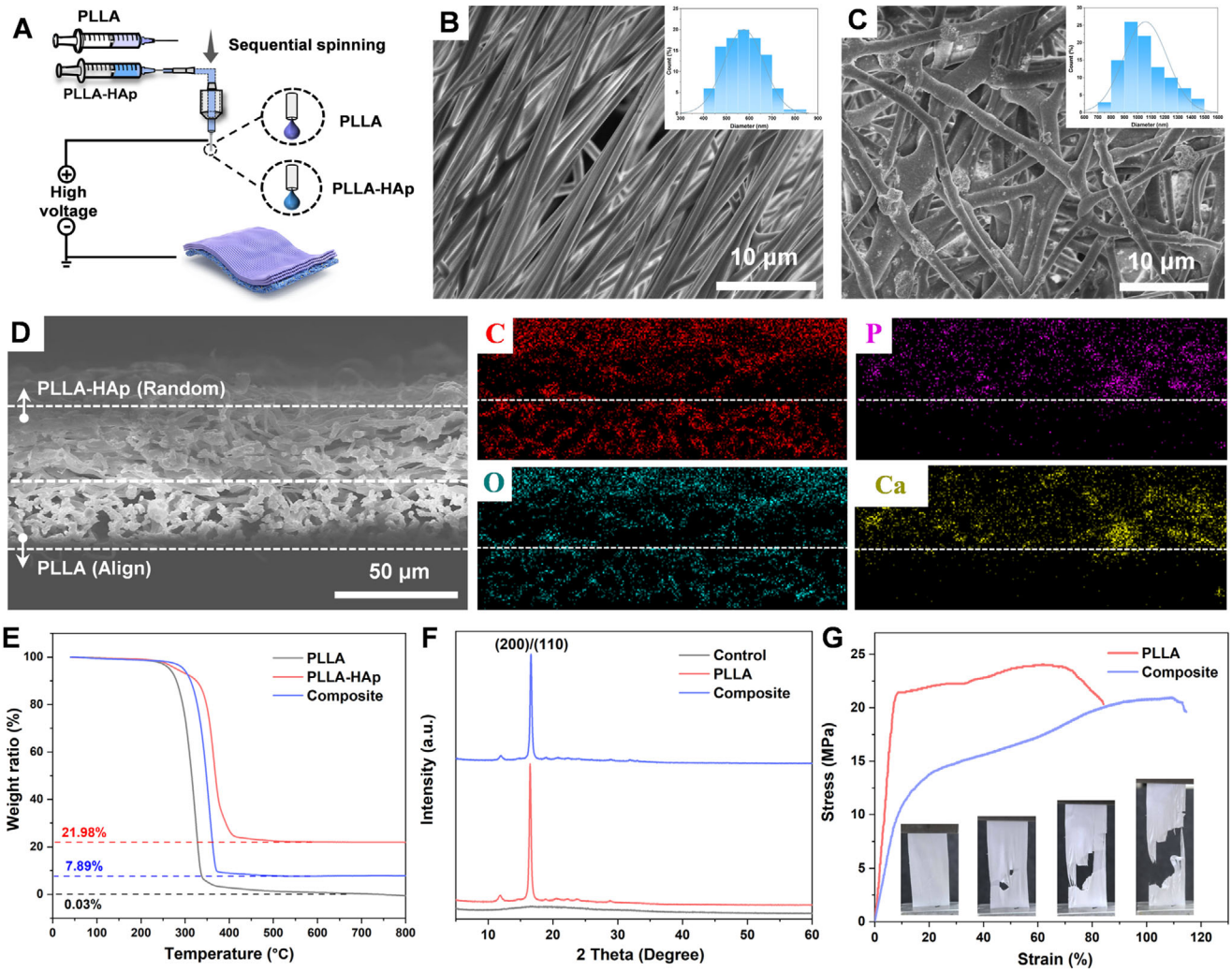

FIGURE 1 | Fabrication and characterization of bilayer piezoelectric nanofiber scaffold. (A) Diagram of sequential spinning of PLLA and PLLA-HAp to prepare a bilayer piezoelectric fiber scaffold. SEM images and fiber diameter statistics of (B) PLLA and (C) PLLA-HAp nanofiber membrane. (D) Cross-section and element distribution of the bilayer piezoelectric fiber scaffold. (E) Thermogravimetric curves of each fiber group. (F) XRD patterns and (G) mechanical properties of PLLA and composite fiber scaffolds.

and this output correlates positively with the frequency of the applied ultrasonic waves (Figure 2C). Considering the presence of PLLA/HAp in the composite scaffold, the piezoelectric performance of PLLA/HAp fiber membranes was also evaluated (Figure S8). However, due to the high concentration of HAp doping, the crystallinity of PLLA is affected (Figure S4), resulting in an output voltage of 0.75 V. The piezoelectric coefficients of both fiber membranes were tested. Compared to the PLLA group, the composite fibers exhibited a decrease in piezoelectric coefficient (Figure S9). This decrease is primarily attributed to the fact that highly concentrated HAp hinders the PLLA's crystallization (Figure S10). Meanwhile, to rule out significant contributions from the intrinsic dielectric properties, the dielectric constants of both the pure PLLA and composite membranes are being measured (Figure S11). HAp doping generally increases the dielectric constant of the composites, but compared to the PLLA fiber, the increase is only slight. Furthermore, to rule out possible triboelectricity, capacitance, or other interfacial effects between the bilayer structures, PLLA-aligned/PLLA-random composite fiber membranes (Pr-Pa) were prepared and tested. The results confirmed that their piezoelectric outputs (~1.21 V, 8.55 nA, and 0.62 nC, respectively) were similar to those of the purely aligned PLLA fibers (Figure S12). Therefore, the structural stress concentration has a more significant impact on the piezoelectric output in the composite scaffold. Based on this, we infer that the HAp dispersed within the random fiber membrane induces a stress concentration effect, thereby triggering the piezoelectric self-enhancement effect in the composite scaffold. The results of the COMSOL simulation confirmed this hypothesis. As shown in Figure 2D, when subjected to external forces, the disordered distribution of HAp can form a more uniform and dense stress distribution around piezoelectric fibers, thereby enhancing electromechanical coupling efficiency. To clarify this mechanism more intuitively and better understand the effect of HAp on the piezoelectric output of PLLA fibers, piezoelectric force microscopy (PFM) phase imaging, Kelvin probe force microscopy (KPFM) surface potential mapping, and local Young's modulus measurements on PLLA and composite fiber membranes were performed (Figure S13). Compared to the PLLA fibers, which exhibited a relatively uniform Young's modulus, the composite

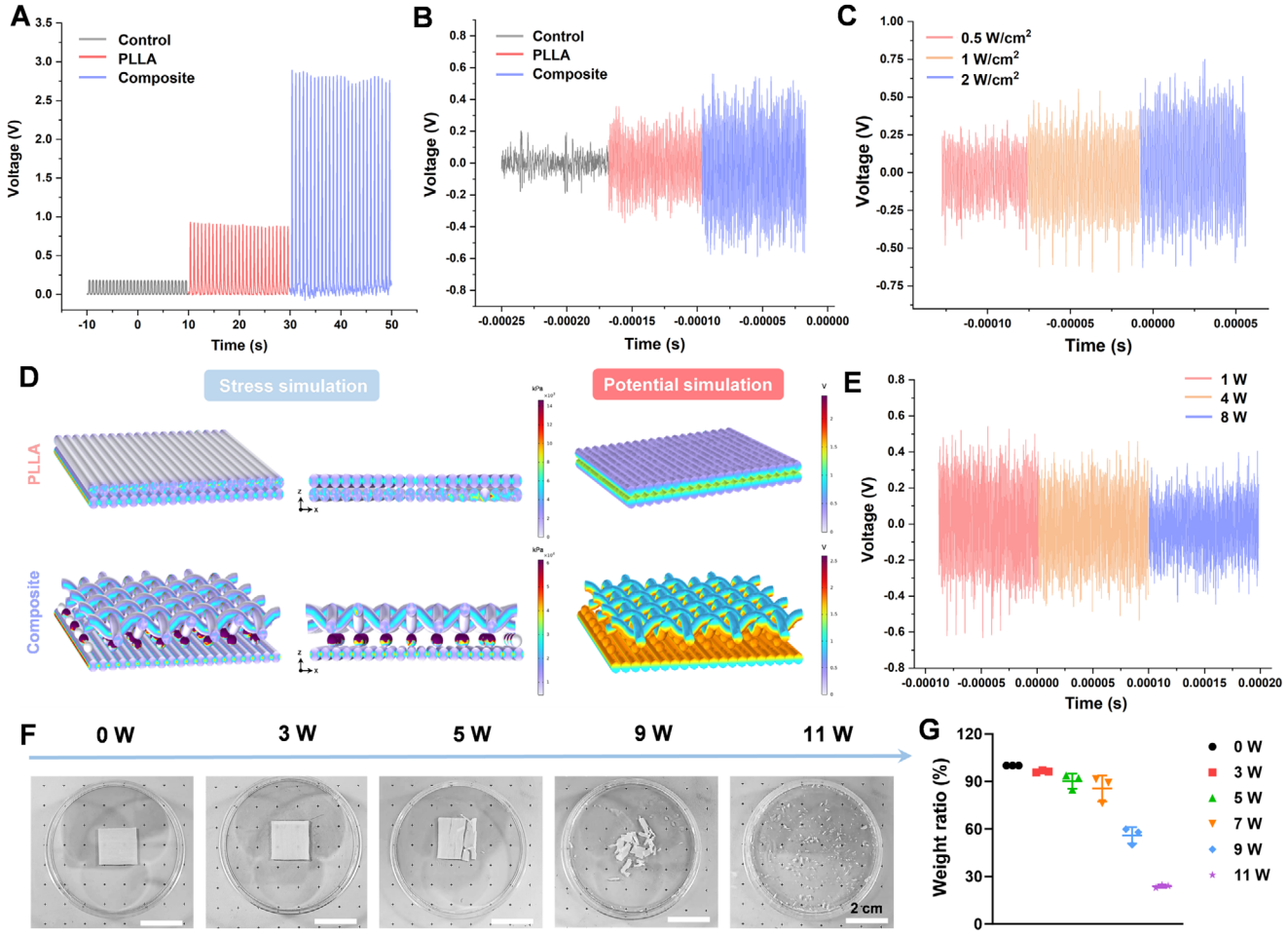

FIGURE 2 | Self-enhanced piezoelectricity and full biodegradability of the bilayer nanofiber scaffold. (A) Electrical output of each nanofiber group under impact mode. (B) Electrical output of each nanofiber group under the US-driven system. (C) Electrical output of the composite fiber scaffold under US-driven conditions at different frequencies. (D) COMSOL analysis of stress and electric potential simulation in the PLLA and composite fiber scaffold. (E) Electrical output of the composite fiber scaffold during different degradation cycles. (F) Digital photographs and (G) mass statistics of the piezoelectric fiber scaffold at different degradation weeks under the 60°C condition.

membrane demonstrated a more heterogeneous distribution of Young's modulus. This heterogeneity in local mechanical properties is a key prerequisite for the formation of stress gradients and helps explain the occurrence of stress concentration phenomena. The composite membrane also exhibited significantly higher local surface potential and more distinct domain reversal (Figure S14). This is consistent with the COMSOL simulation results.

2.3 | Fully Biodegradable Property of Bilayer Piezoelectric Nanofiber Scaffold

Due to PLLA being a biodegradable piezoelectric polymer, the bilayer piezoelectric scaffold gradually degrades during musculoskeletal regeneration and progressively transfers mechanical load to the newly formed TBI. Degradation of the bilayer nanofiber scaffold proceeds slowly at 37°C, with noticeable cleavage occurring by week 15 (Figure S15). By week 30, it retains 65% of its initial weight (Figure S16). SEM images reveal that the bilayer nanofiber scaffold maintains most of its fibrous structure at week 8 (Figure S17). Simultaneously, the piezoelectric output of the bilayer piezoelectric scaffold was evaluated at weeks 1, 4, and 8 during the degradation period. Although a decreasing trend appeared, it maintained a favorable and sustained piezoelectric output performance (Figure 2E). To further evaluate the full biodegradability of the bilayer piezoelectric scaffold, we observed its degradation behavior under a heating regimen at 60°C. As shown in Figure 2F, significant cracking occurred by week 5, and the scaffold was barely detectable by week 11, with its mass reduced to only 22% of the initial mass. This result indicated that subsequent animal experiments will not require a second surgery to remove the implanted scaffold.

2.4 | Biocompatibility and Proliferation on Piezoelectric Scaffolds

To evaluate the biocompatibility of the scaffolds and the effects of piezoelectric stimulation on cell proliferation on scaffolds (Figure 3A), in vitro experiments were divided into four groups: PLLA layer without US (PLLA-US), PLLA layer with US stimulation (PLLA + US), PLLA-HAp layer without US (PLLA-HAp-US), and PLLA-HAp layer with US (PLLA-HAp + US). The group

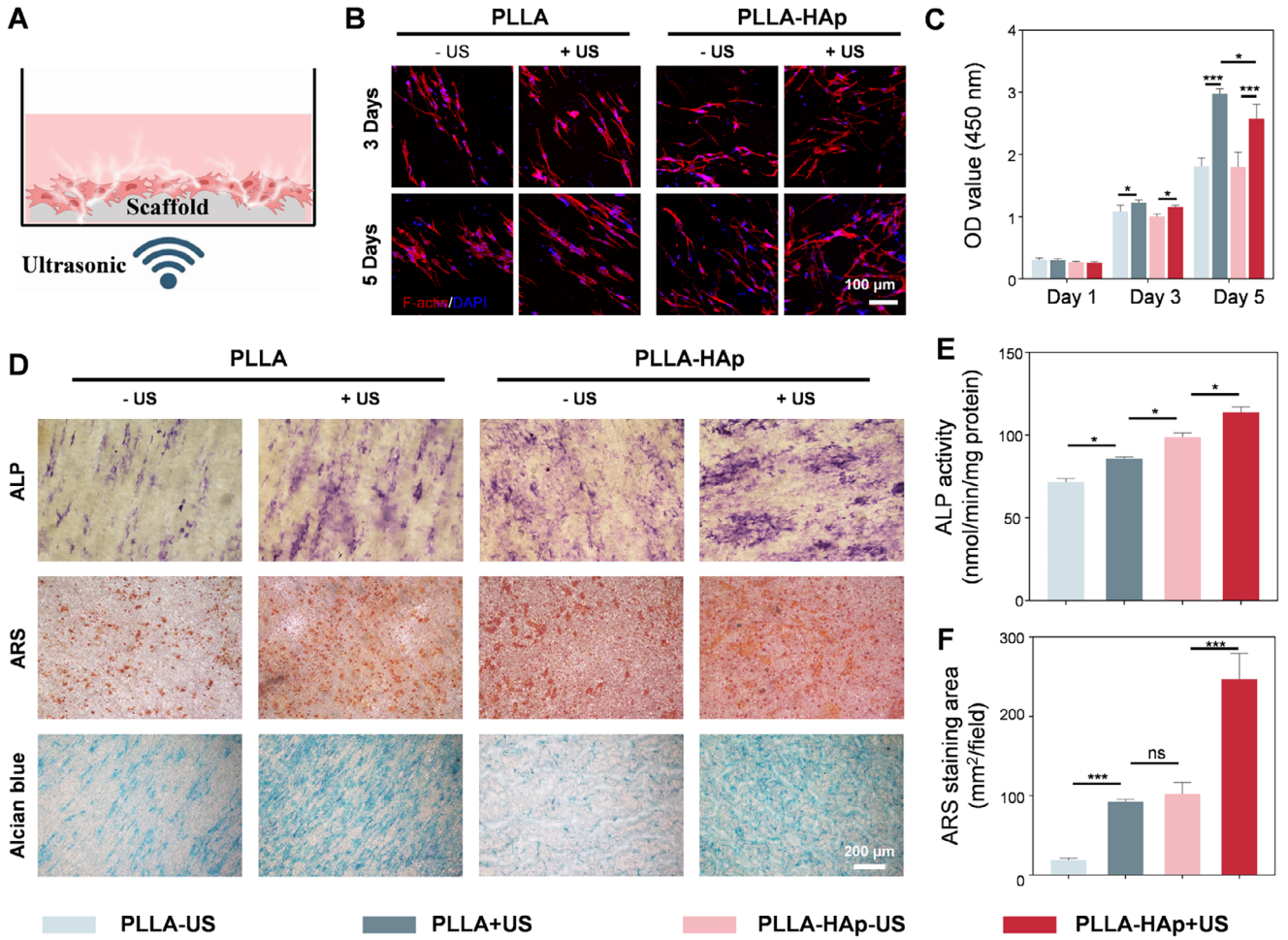

FIGURE 3 | US-activated piezoelectric effect promotes BMSCs proliferation and differentiation. (A) Diagram of US-mediated electrical stimulation in cell experiments. (B) Confocal microscopy images of BMSCs spreading on different fiber membranes (with/without US simulation). (C) Cell proliferation on the different types of scaffolds. (D) Digital photographs of ALP, ARS, and Alcian blue staining of the differentiated cells after culturing MSCs on the various types of scaffolds for 7, 14, and 7 days, respectively. Quantitative analysis of (E) ALP activity and (F) ARS staining area. (*$p < 0.05$, **$p < 0.01$, and ***$p < 0.001$).

treated with US for 2 min per day (0.5 W/cm^2) did not cause additional thermal damage to the cell culture under these conditions (Figure S18). Figure S19 showed the live/dead staining on days 3 and 5 revealed a high proportion of viable cells in all groups, with negligible cell death observed on both PLLA and PLLA-HAp layers, regardless of US stimulation. Furthermore, cells cultured on the PLLA layer consistently exhibited an aligned morphology, whereas those on the PLLA-HAp layer showed a random distribution (Figure 3B). The application of the US did not alter cell growth or arrangement on either fiber topology.

The effect of US stimulation on cell proliferation was quantified by CCK-8 assay on days 1, 3, and 5 (Figure 3C). On day 1, no significant differences were observed among all groups. On day 3, US stimulation had significantly promoted cell proliferation on both scaffold layers, with no difference between the PLLA + US and PLLA-HAp + US group. On day 5, the pro-proliferative effect of US was more pronounced, and the proliferation rate had no significant difference between the PLLA-US and PLLA-HAp-US groups.

2.5 | US-Activated Piezoelectric Effect Promotes BMSCs Differentiation

Considering the specificity of TBI regeneration, we systematically evaluated the synergistic effects of US-activated ES and a bilayer piezoelectric scaffold on BMSCs differentiation, encompassing the tenogenic, chondrogenic, and osteogenic differentiation capabilities.

To evaluate the osteogenic potential of the scaffold, early osteogenesis ability was first assessed by alkaline phosphatase (ALP) activity and staining. After culturing for 7 days, Figure 3D,E showed that ALP activity was significantly higher on the PLLA-HAp layer than on the PLLA layer. Following US stimulation, the osteogenic differentiation of BMSCs was significantly enhanced on both layers, with the PLLA-HAp + US group exhibiting the highest early osteogenic activity. This trend was further confirmed by ARS staining after 14 days, where the PLLA-HAp+US group formed larger areas of calcium nodules, indicating the strongest late-stage mineralization capacity (Figure 3F). However, Alcian blue staining revealed no significant differences

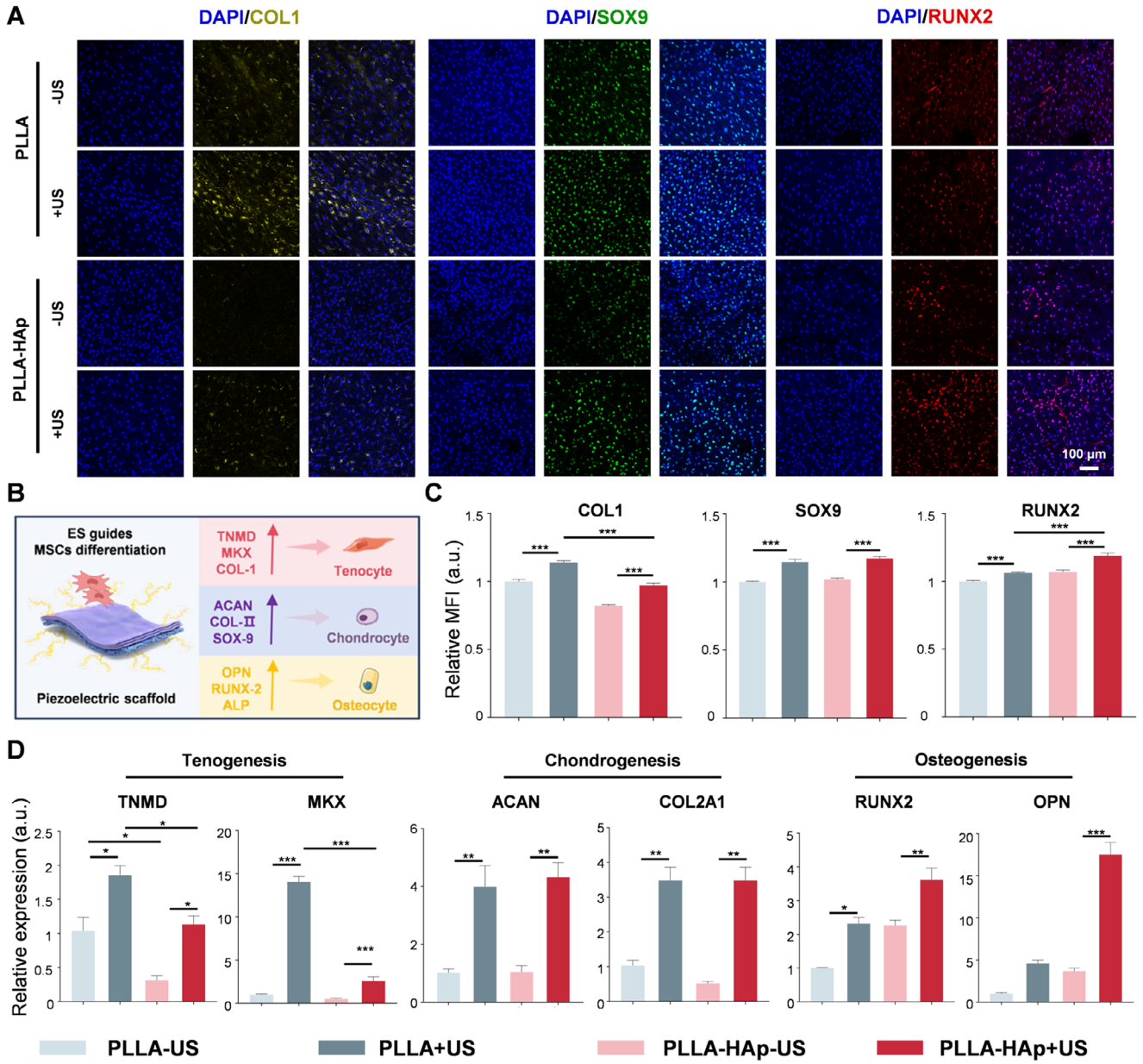

FIGURE 4 | ES guides tri-lineage differentiation of BMSCs on the piezoelectric scaffold in vitro. (A) Immunofluorescent staining of tenogenic (COL1), chondrogenic (SOX9), and osteogenic markers (Runx-2), after culturing BMSCs for 7 days, respectively, on the different types of scaffolds. (B) A schematic diagram illustrating the combined guidance of ES cells and scaffolds for the directed differentiation of MSCs and expression of related proteins. (C) Statistical analysis of the mean fluorescence intensities of COL1, SOX9, and Runx-2, by measuring the images' mean pixel intensity (MPI). (D) The relative expressions of representative tenogenesis genes (TNMD, MKX), chondrogenesis genes (ACAN, COL2A1), and osteogenesis genes (Runx-2, OPN) of the differentiated cells after culturing BMSCs for 7 days on the different types of scaffolds. (*$p < 0.05$, **$p < 0.01$, and ***$p < 0.001$).

between the two scaffold layers, but the application of US promoted an increase in positive areas.

To further validate the regulatory capacity of the upper and lower layers of the scaffold and the piezoelectric effect on tendonogenic, chondrogenic, and osteogenic differentiation specificity, we measured the expression of relevant proteins and genes associated with different differentiation pathways (Figure 4A,B). For tendonogenic differentiation, the PLLA layer showed superior tenogenesis potential. Immunofluorescence staining showed that the expression of collagen type I (COL1) was significantly higher on the PLLA layer, and US enhanced expression in all groups, while the PLLA + US group remained the highest expression (Figure 4A,C). qPCR results showing that tenogenic markers (TNMD and MKX) were more highly expressed on the PLLA layer and were further enhanced by piezoelectric stimulation (Figure 4D). Regarding chondrogenic differentiation, no significant difference was observed between the two scaffold layers. Immunofluorescence for SOX9 and qPCR for chondrogenic genes (ACAN and COL2A1) consistently showed that while there was no difference between the PLLA and PLLA-HAp surface, piezoelectric stimulation significantly promoted the expression of all chondrogenic markers (Figure 4A,D). Regarding osteogenic differentiation, immunofluorescence staining for

osteogenesis-related RUNX2 revealed superior expression on the PLLA-HAp layer, which was significantly upregulated by piezoelectric stimulation (Figure 4C). Expression of osteogenic genes (RUNX2 and OPN) also supported this finding (Figure 4D). To eliminate the effects of the US, non-piezoelectric polylactic acid (PLA) fiber membranes and PLA-HAp fiber membranes were prepared to measure their voltage output (<0.05 V) (Figure S20). Among the results of different lineage differentiation, the direct US stimulation on the PLA and PLA-HAp scaffold did induce a modest increase in differentiation markers compared to the non-US control; the piezoelectric PLLA-based scaffold under the same US stimulation consistently resulted in significantly higher expression levels of all lineage-specific markers (Figure S21). These results indicate that the enhanced differentiation capacity stems primarily from the electrical signals generated by the piezoelectric effect of the PLLA-based scaffold upon US activation, rather than solely from the direct mechano-stimulation of the US.

To investigate the regulation of cartilage regeneration at the interface, a bilayer heterogeneous fiber membrane consisting of aligned PLLA fibers on one side and disordered PLLA-HAp fibers on the other was prepared (Figure S22). The results showed a gradient distribution of COL-X at the interface. Specifically, at the interface of the bilayer scaffold, we observed significantly higher levels of COL-X expression in the PLLA-HAp layer. In contrast, expression levels in the PLLA layer were relatively low. This trend was more pronounced after US treatment (Figure S23). This confirms that the PLLA-HAp layer actively promotes the differentiation of MSCs into a calcified chondrocyte phenotype via HAp-induced mineralization signals. Based on this, we subsequently selected PLLA-HAp for studies on chondrogenic differentiation (mineralization) and PLLA for studies on chondrogenic differentiation (non-mineralization).

2.6 | Mechanism of the Piezoelectric Effect Guiding Tri-Lineage Differentiation of BMSCs

To elucidate the mechanism of piezoelectric stimulation in the differentiation of BMSCs (Figure 5A), we performed RNA-sequencing in the following groups with and without US stimulation: tenogenic (PLLA layer), non-mineralized chondrogenic (PLLA layer), mineralized chondrogenic (PLLA-HAp layer), and osteogenic (PLLA-HAp layer).

Differential gene expression (DEG) analysis revealed that US stimulation significantly altered gene expression: 172 up-regulated genes and 49 down-regulated genes in the tenogenic group, 140 up-regulated genes and 66 down-regulated genes in the non-mineralized chondrogenic group, 91 up-regulated genes and 94 down-regulated genes in the mineralized chondrogenic group, 11 up-regulated genes and 15 down-regulated genes in the osteogenic group (Figure 5B). KEGG enrichment analysis was also performed to elucidate the functional roles of these DEGs. Remarkably, the PI3K-AKT signaling pathway was enriched in all groups (Figure 5C–F). A heatmap of genes within the PI3K-AKT pathway also confirmed this enrichment (Figure S24). The analysis also highlighted lineage-specific pathways pertinent to each fate, such as the MAPK and VEGF pathways in the tenogenic group, the AMPK pathway in the non-mineralized chondrogenic group, the Rap1 and Hedgehog pathways in the mineralized chondrogenic group, and the Wnt and AMPK pathways in the osteogenic group. Given its consistent enrichment across groups, we performed Gene Set Enrichment Analysis (GSEA) to validate the pivotal role of the PI3K-AKT pathway (Figure S25), which confirmed that the pathway was significantly activated in response to US stimulation across all groups. Western blot analysis revealed that, across all relevant differentiation lineages, levels of p-AKT and p-PI3K were upregulated following US treatment, while the protein levels of PI3K and AKT remained consistent. This directly confirms that piezoelectric stimulation indeed activates the PI3K/AKT pathway at the protein level (Figure 5G). Furthermore, differentiation results following inhibitor addition (Figure S26) indicate that when the PI3K/AKT pathway is inhibited, lineage-specific differentiation markers are consistently suppressed. These results suggest that the PI3K/AKT pathway plays a critical role in mediating the effects of US-activated piezoelectric stimulation on MSCs differentiation toward tenogenic, chondrogenic, and osteogenic lineages.

2.7 | US-Activated Piezoelectric Stimulation Facilitates Functional Recovery in the RCT Model

Given the significant TBI healing potential of the scaffold in vitro, we further established a RCT model to evaluate the regenerative effects of piezoelectric stimulation (Figures 6A and S27). Rats were randomly divided into four groups: suture-only without US (Suture-US), suture-only with ultrasound (Suture + US), scaffold implantation without ultrasound (Scaffold-US), and scaffold implantation with ultrasound (Scaffold + US). Functional and histological evaluations were conducted at 4 and 8 weeks post-surgery. To avoid thermal effects, the local temperature was monitored using an infrared thermal camera during the US application to eliminate thermal influences (Figure 6B). Functional recovery was first evaluated based on gait analysis (Figure 6C). At 4 weeks post-surgery, the Suture-US group exhibited the shortest stride length. In comparison, US intervention significantly increased the stride length in the suture-only condition (Suture + US). The Scaffold-US resulted in a greater improvement in stride length compared with the Suture + US group, while the Scaffold + US group achieved the longest stride length, indicating the best early functional recovery (Figure 6F). By 8 weeks post-surgery, all groups showed significant improvement in stride length compared to the 4-week repair. The Suture-US group still had the shortest stride length, whereas no significant difference was observed between the Suture + US and Scaffold-US groups. Nevertheless, the Scaffold + US group still had the longest stride length.

2.8 | US-Activated Piezoelectric Stimulation Promotes Tissue Repair in the RCT Model

Subsequently, we evaluated the histology of regenerated TBI tissue. Micro-CT analysis revealed a consistent trend in bone regeneration at the tendon–bone interface at both 4 and 8 weeks (Figure 6D). For suture-only groups, US application did not significantly alter the bone volume fraction (BV/TV) in the

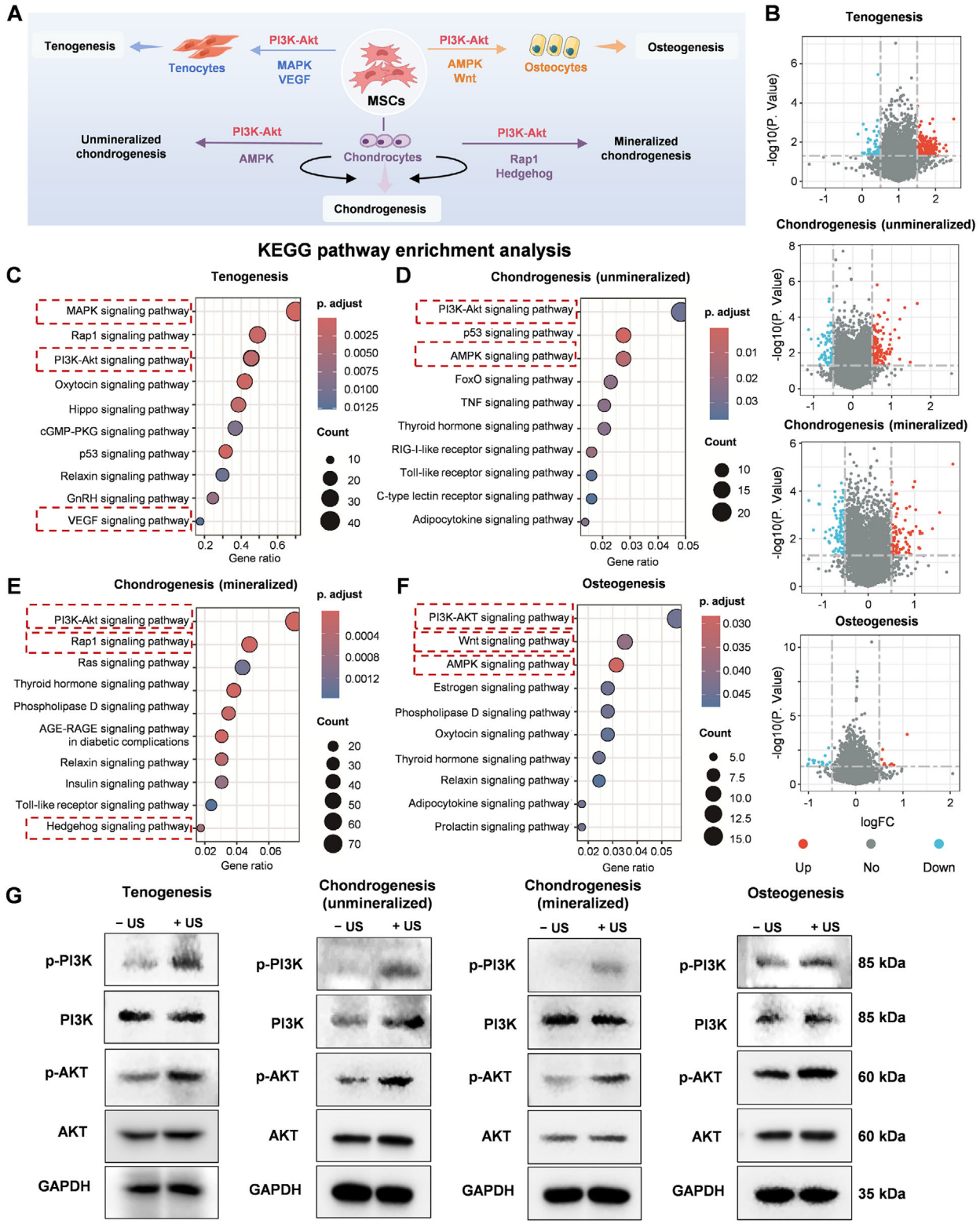

FIGURE 5 | Transcriptome analysis of tri-lineage differentiation of BMSCs. (A) The pathways and potential mechanisms of MSCs' directed differentiation on different scaffolds (with or without ES). (B) DEG analysis for the tenogenic group, the non-mineralized chondrogenic group, the mineralized chondrogenic group, and the osteogenic group with and without US stimulation, respectively. KEGG enrichment analysis of (C) the tenogenic group, (D) the non-mineralized chondrogenic group, (E) the mineralized chondrogenic group, and (F) the osteogenic group. (G) Western blotting analysis of PI3K, p-PI3K, AKT, and p-AKT in various groups.

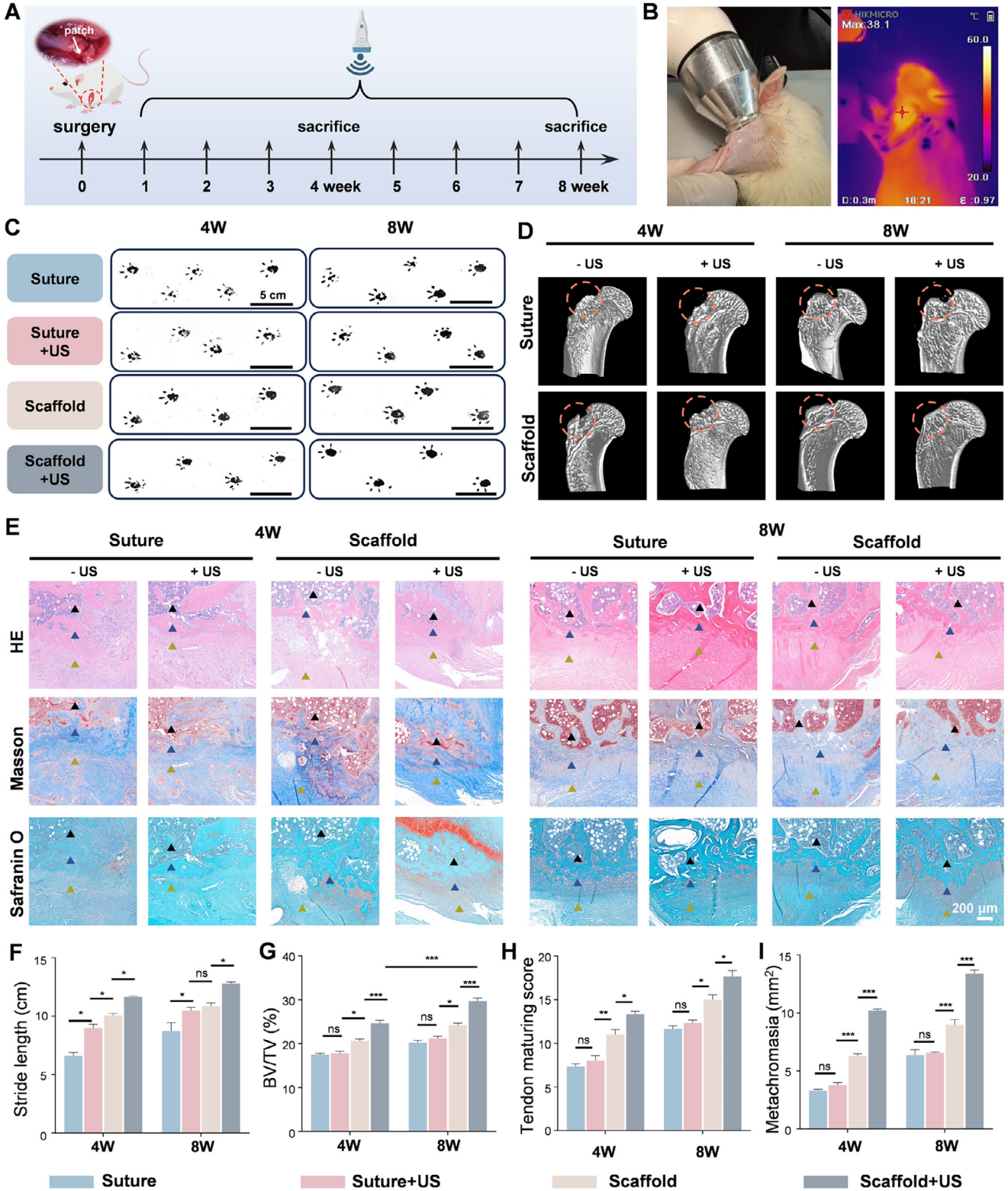

FIGURE 6 | US-Activated piezoelectric stimulation facilitates functional recovery and tissue remolding in the RCT model. (A) Depict the procedures for animal experimentation and postoperative harvesting procedures. (B) A digital photograph of the rat undergoing US stimulation and the subsequent thermal imaging. (C) Footprint data of the different groups at 4 and 8 weeks. (D) Micro-CT images of the repaired rotator cuff tissue at 4 and 8 weeks post-operation. The pink dashed circles indicate the original defect borders. (E) H&E, Masson's trichrome, and Safranin O/Fast Green staining of the different groups at 4 and 8 weeks, respectively. The black arrow indicates bone tissue, the blue arrow indicates TBI tissue, and the green arrow indicates tendon tissue. Quantitative measurements of (F) stride length, (G) BT/TV (%), (H) tendon maturing score, and (I) fibrocartilage metachromasia. (*$p <$ 0.05, **$p < 0.01$, and ***$p < 0.001$).

footprint area. However, BV/TV was markedly increased in the Scaffold-US group, and the most robust bone regeneration was observed in the Scaffold + US group (Figure 6G). Furthermore, the BV/TV in all groups was higher at 8 weeks than at 4 weeks, indicating progressive enhancement of bone formation over time.

Hematoxylin and Eosin (H&E), Masson's trichrome, and Safranin O (SO)/Fast Green staining were used to further evaluate the histological characteristics of newly formed TBI tissue (Figure 6E). No significant inflammatory cell infiltration was observed in any group post-surgery. At 4 weeks postoperatively, the healing interface in the suture-only groups (Suture-US and Suture + US) exhibited sparse cellularity, disorganized and loosely arranged collagen fibers, and thin layers of primary fibrocartilage formation at the healing interface, with no significant differences between the Suture-US and Suture + US groups. In contrast, the Scaffold + US group showed more abundant cell proliferation, better-organized collagen fibers, and initial fibrocartilage formation compared to the Scaffold-US group. At 8 weeks postsurgery, though there was a significant improvement compared to 4 weeks post-surgery, the healing of TBI in the suture-only groups remained suboptimal, with no significant improvement after US intervention. While the healing quality improved further in both scaffold-implanted groups, the Scaffold + US group displayed the most mature tissue architecture. The modified tendon-maturing score confirmed that US intervention had no significant effect on the suture-only groups (Figure 6H). The Scaffold-US group had a higher repair score than the suture-only repair, and the Scaffold + US group achieved the most favorable score. In addition, quantitative analysis of the fibrocartilage metachromasia area aligned with histological scoring results (Figure 6I).

2.9 | US-Activated Piezoelectric Stimulation Promotes TBI Integration

To comprehensively evaluate the integration of the regenerated TBI, biomechanical recovery and tissue remodeling were thoroughly assessed (Figure 7A). After performing tensile tests on the samples from each group, it was found that a consistent trend for both ultimate load and stiffness was observed in all groups at the 4- and 8-week time points (Figure 7B,C). In the suture-only groups, US application did not significantly increase the ultimate load but effectively increased stiffness. The scaffold implantation groups demonstrated superior ultimate load and stiffness compared with the suture-only groups, even without US applied. The Scaffold + US group achieved the highest values for both ultimate load and stiffness among all groups.

At the histological level, the most organized and dense collagen fiber alignment was observed at the TBI site in the Scaffold + US group under polarized light microscopy (Figure 7D). Immunohistochemical staining for collagen type II (COL II) showed that the Scaffold + US group endows the most extensive positive staining area, indicating the strongest fibrocartilage regeneration (Figure 7E). The Scaffold-US group also had a notable cartilage regeneration ability, while no significant difference was observed between the Suture-US and Suture + US groups (Figure 7H). We also assessed the scar formation in TBI through α-SMA staining (Figure 7F). The results showed significant α-SMA expression in both Suture-US and Suture + US groups, suggesting pronounced scar formation during TBI repair without scaffold intervention. Conversely, α-SMA expression was markedly reduced in the Scaffold-US group, with the lowest expression in the Scaffold + US group, indicating that piezoelectric stimulation can effectively suppress scar formation at the TBI (Figure 7I). Moreover, dual immunofluorescence staining for Col2A1 and OCN showed that the Scaffold + US group had abundant COL2A1 expression and exhibited the most prominent OCN expression at the TBI site, suggesting a satisfactory state of cartilage and bone regeneration (Figure 7G,J). Overall, this piezoelectric scaffold not only provides mechanical support and a physicochemical microenvironment for cells but also delivers ES to guide MSCs toward differentiation in distinct regions, achieving synchronized regeneration of the TBI.

3 | Discussions

The complex native architecture of TBI makes it difficult to establish an appropriate biochemical microenvironment without external intervention once the interface is damaged. Therefore, designing suitable scaffolds is crucial for promoting the migration, proliferation, and signaling of regenerative cells [14]. In this study, the piezoelectric scaffold is designed to mimic the unique architecture of TBI, providing mechanical support and physicochemical microenvironment for cells. Meanwhile, it can deliver ES to guide MSC differentiation across different regions, thereby achieving synchronized regeneration of the TBI. First, the bilayer fiber scaffold incorporates both aligned fibers (providing topological cues mimicking tendon structure) and random fibers (promoting osteoblast growth and differentiation). It also possesses the characteristic β-crystalline phase of PLLA, resulting from the orientation of C═O dipoles within the PLLA molecular chains during annealing. The mechanical properties of the scaffold are critical for healing at the TBI. The scaffold must possess adequate strength and toughness to withstand the tensile forces generated by tendon movement and prevent premature failure due to insufficient mechanical performance [24]. The bilayer fiber scaffold showed ideal flexibility and strength, attributable to the composite of oriented and random fibers. And the existing mechanical properties are sufficient to meet the requirements of the rotator cuff patch.

In constructing bionic scaffolds for rotator cuff repair, previous research has primarily focused on material modification and the loading of bioactive factors, while studies on restoring the physiological electro-microenvironment remain insufficient [28]. It is also a major challenge to reshape the electro-microenvironment of rotator cuff tissue and spatially regulate the differentiation direction of MSCs to facilitate TBI remodeling [3]. Based on PLLA fibers, the piezoelectric performance of the prepared bilayer fiber scaffold is three times that of pure PLLA. This addresses the inherent limitation of insufficient piezoelectric properties in traditional PLLA while introducing a calcium phosphate reservoir essential for bone regeneration. More interestingly, this phenomenon does not arise from simple coupling or the HAp doping enhancing the crystallinity of PLLA, but rather from stress concentration effects caused by the disordered distribution of PLLA/HAp fibers on the aligned PLLA fiber matrix [41].

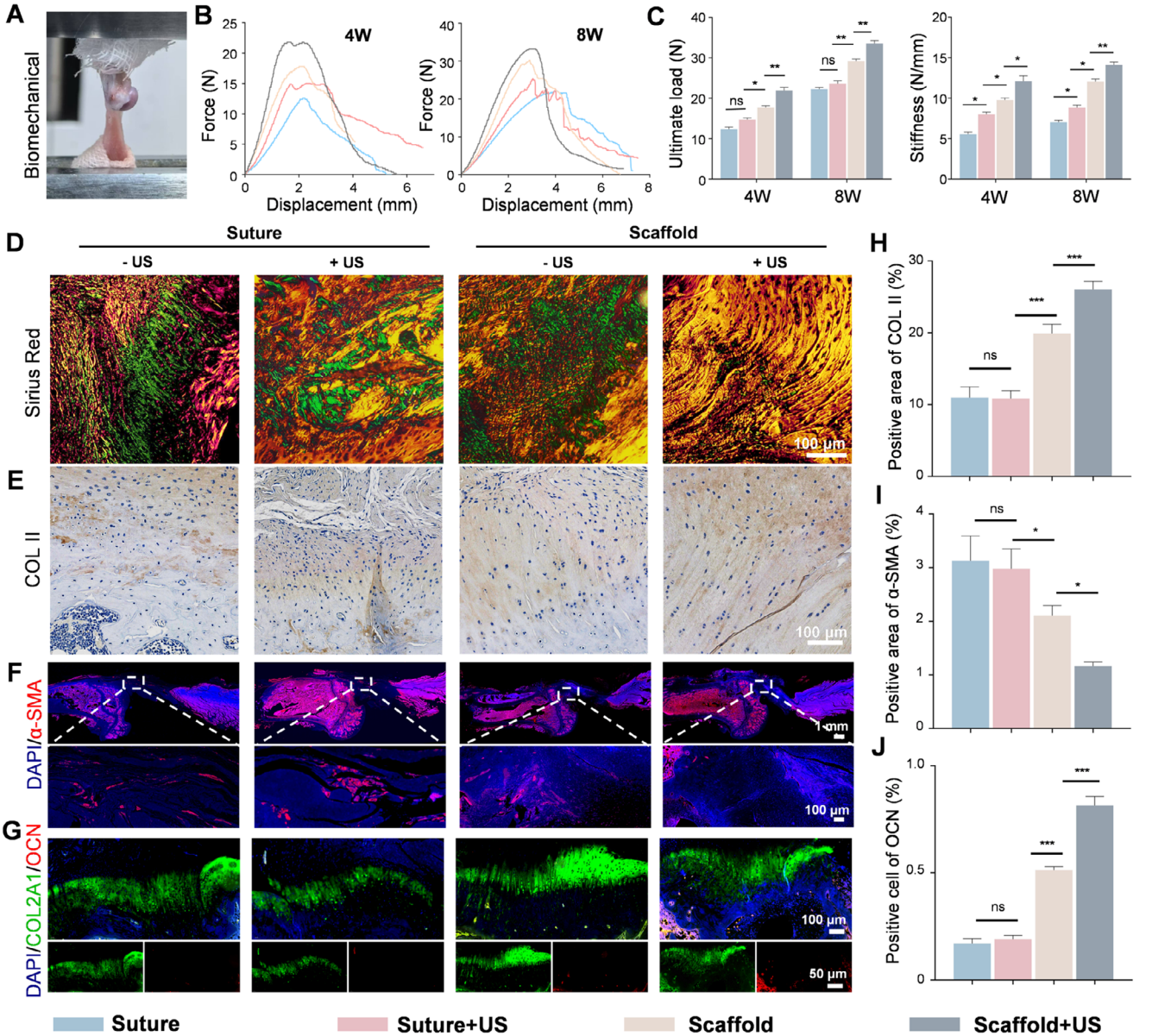

FIGURE 7 | US-Activated piezoelectric stimulation promotes TBI integration. (A) The digital photographs of biomechanical testing on rotator cuff samples. (B) Force–displacement curves, (C) ultimate failure load and stiffness for each group at 4 and 8 weeks. (D) Sirius Red staining (yellow: COL I; green: COL III), and (E) COL II staining at 8 weeks post-operation after implantation with different scaffolds. Immunofluorescence staining of (F) α-SMA (red color), (G) Col2A1 (green color), and OCN (red color) at 8 weeks. Quantitative analysis of (H) COL II, (I) α-SMA, and (J) OCN expression positive areas, respectively. (*$p < 0.05$, **$p < 0.01$, and ***$p < 0.001$).

The microscopic observation directly supports the hypothesis. Under external mechanical stimulation, these concentrated stress fields locally amplify the external stimuli acting on the PLLA fibers, thereby enhancing the electromechanical responses and piezoelectricity. Moreover, the sustained piezoelectric output demonstrated within 8 weeks assures subsequent animal studies. It also demonstrated full biodegradability, thereby eliminating the need for secondary surgery.

In vitro, the pro-proliferative experiments showed that the PLLA layer was significantly superior to the PLLA-HAp layer in the US groups. This may be attributed to the synergistic proliferation promotion effect between the piezoelectric stimulation and the aligned morphology of the PLLA [33]. The Janus structure plays a key role in promoting directional differentiation. The aligned structure of PLLA and the random structure of PLLA-HAp mimic the ECM distribution at the native TBI, enhancing the capacity for directed differentiation toward tendon and bone, respectively [42, 43]. Concurrently, the intrinsic osteogenic properties of HAp within the PLLA-HAp layer further augment osteogenic differentiation [44]. Given that fibrocartilage regeneration is critical for TBI regeneration [45, 46], we also evaluated the scaffold's effect on promoting chondrogenesis. Notably, neither layer showed superior chondrogenic potential over the other, regardless of US stimulation. This suggests that chondrogenic differentiation is less regulated by the scaffold topography, whereas the effect of ES is pronounced. Although US-activated piezoelectric stimulation promoted chondrogenesis on both layers, the regenerated

cartilage phenotype differed. The HAp in the PLLA-HAp layer mimics a mineralized microenvironment, preferentially inducing calcified cartilage regeneration [47]. In contrast, the PLLA layer lacks mineralization signals and thus tends to induce non-calcified cartilage regeneration [48]. This gradient corresponds to the structural gradient of the native TBI, which is expected to facilitate integration of the TBI.

In investigating the regulatory role of ES-coupled bilayer piezoelectric scaffold on three-lineage differentiation, RNA sequencing revealed that the PI3K-AKT signaling pathway was activated in all four differentiation lineages (tenogenesis, unmineralized chondrogenesis, mineralized chondrogenesis, and osteogenesis). This indicates that the PI3K-AKT pathway is the central mediator of the BMSC response to piezoelectric stimulation [29, 49]. The PI3K-AKT pathway is known as a major pathway that responds to mechanical stimulation, regulating cell proliferation and metabolism, thereby influencing stem cell fate [50, 51]. For different lineages, piezoelectric stimulation also induces directional differentiation by activating specific guiding pathways, including: MAPK and VEGF (tenogenesis) [52, 53], AMPK (unmineralized chondrogenesis) [54], Rap1 and Hedgehog (mineralized chondrogenesis) [55, 56], and Wnt and AMPK (osteogenesis) [57, 58].

In vivo, US stimulation alone failed to show significant histological or functional improvement. A slight improvement in the gait of rats was observed, which may be related to the pain relief effect of US [59]. In contrast, the Scaffold-only group exhibited favorable tissue regeneration. We hypothesize that this might be attributed to weak, intermittent piezoelectric stimulation generated by the daily activities. The scaffold with the US group, which received regular piezoelectric stimulation, achieved the optimal regenerative outcome. Furthermore, piezoelectric stimulation not only effectively accelerated tissue regeneration but also significantly reduced local tissue fibrosis and promoted the regular alignment of regenerated fibers, thereby further improving the quality of repair.

4 | Conclusion

In summary, we have successfully developed a fully biodegradable piezoelectric fiber scaffold for repairing rotator cuff tears, addressing the critical challenge of multi-tissue regeneration at the TBI site. Through the rational design of its structural components, this scaffold ingeniously harnesses a piezoelectric enhancement effect via stress concentration. This dynamic ES signaling effectively activates the PI3K/AKT pathway, enabling spatiotemporal control over the differentiation of the desired tenogenic, chondrogenic, and osteogenic lineages. Remarkably, in a rat RCT model, the integration of this topological scaffold with US-driven ES successfully addressed the challenging triphasic tissue repair at the TBI site, achieving synchronized repair of tendon, cartilage, and bone. Importantly, the fully biodegradable scaffold was constructed from simple components, eliminating the risk of secondary surgery, allowing flexibility in fabrication and clinical adaptation. This work also provides a foundational framework for developing next-generation scaffolds for interfacial tissue engineering and other complex regenerative contexts.

5 | Experimental Section

5.1 | Materials and Chemicals

PLLA and PLA were obtained from Esunmed (Shenzhen, China). Hydroxylapatite (HAp) was purchased from Macklin Biochemical Technology Co., Ltd. (Shanghai, China). Hexafluoroisopropanol (HFP, 99.5%) was purchased from Aladdin Biochemical Technology Co., Ltd. (Shanghai, China). α-MEM (M3402), phosphate buffered solution (PBS, P1022), ascorbic acid (A8100), dexamethasone (D8040), Trypsin-EDTA solution (T1300), Penicillin–streptomycin liquid (PS, P1400), DAPI resolution (C0060), cell counting kit-8 (CCK-8, CA1210), alkaline phosphatase stain kit (G1481), and alizarin red S solution (G1450), β-glycerophosphate (G1485) were purchased from Solarbio Science & Technology Co., Ltd. Alkaline phosphatase assay kit (P0321S), Alcian blue solution (C0155S), 4% paraformaldehyde (PFA) (P0099) were purchased from Beyotime Biotechnology. Collagen type I monoclonal antibody (66761-1-Ig), COL10A1 (COL-X) antibody, and osteocalcin polyclonal antibody (23418-1-AP) were purchased from Proteintech. Phalloidin-iFluor 555 (ab176756), goat anti-rabbit IgG H&L (ab150077), and anti-SOX9 antibody (ab185966) were purchased from Abcam. Alpha-smooth muscle actin monoclonal antibody (MA1-06110) was purchased from Invitrogen. Sodium pyruvate (P5280) and 2-phospho-L-ascorbic acid (49752) were purchased from Sigma-Aldrich. TGF-β3 (HY-P7120) and LY294002 (HY-101080) were purchased from MedChemExpress. ITS cell culture supplement (ITSS-10201) was purchased from Oricellbio. The fetal bovine serum (FBS) was purchased from Gibco. RUNX2 Rabbit mAb and Phospho-PI3 Kinase p85/p55 antibody were purchased from Cell Signaling Technology. Akt (pan) antibody, Phospho-Akt (Ser473) antibody, and PI3 Kinase p85 antibody were purchased from Selleck. Col2A1 antibody (M2139) was purchased from Santa Cruz Biotechnology.

5.2 | Fabrication and Characterization of Bilayer Nanofiber Scaffold

First, the electrospinning solutions were prepared by dissolving PLLA (10 w/v%) and PLLA/HAp (10 w/v% and 3 w/v%) in HFP. Then the solution was electrospun at a flow rate of 1 mL/h under a voltage of 15 kV, with a tip-to-collector distance of 15 cm. A rotating drum collector operating at 2000 rpm to obtain the aligned nanofiber membrane (PLLA), while operating at 200 rpm to obtain the random nanofiber membrane (PLLA-HAp). The bilayer nanofiber membrane integrates an aligned PLLA membrane with a random PLLA-HAp membrane through a sequential electrospinning technique. Similarly, PLA (10 w/v%) and PLA/HAp (10 w/v% and 3 w/v%) spinning solutions were also used to produce PLA fiber membranes via electrospinning. Subsequently, all scaffolds were annealed in a 150°C oven for 12 h, yielding the final piezoelectric scaffold.

The morphologies of the nanofiber scaffolds were characterized by scanning electron microscopy (SEM, SU8020, Japan), and the diameter of the fibers was quantified using the ImageJ software according to the SEM images. Elemental mapping was performed to verify the distribution of HAp within the composite nanofibers. Fourier-transform infrared (FTIR) spectroscopy (Nicolet 8700, Bruker) was used to analyze the changes in

the chemical composition of the PLLA and PLLA-HAp membranes. Thermogravimetric analysis (TGA) was conducted to evaluate the component ratios of each fiber scaffold under a nitrogen atmosphere. A plasma cleaner (GD-5, FARI Plasma) is used to treat fiber membranes on the surface to enhance their hydrophilicity. The hydrophilic properties were assessed by measuring the contact angle using a contact angle tester. The crystalline structure of the nanofiber scaffolds was determined using an x-ray diffractometer (XRD). The fiber crystallization ability was tested using a differential scanning calorimeter (DSC). The tensile properties of the scaffolds were evaluated using an ESM301/Mark-10 tensile testing system with a sample size of 3×1.5 cm and a tensile speed of 5 mm min^{-1}.

5.3 | Piezoelectric Properties and Degradability of Bilayer Nanofiber Scaffolds

A piezoelectric constant measuring instrument (ZJ-6BN) was used to test the piezoelectric coefficients of each group of fiber membranes. Piezoelectric force microscopy (PFM) phase imaging, Kelvin probe force microscopy (KPFM) surface potential mapping, and local Young's modulus measurements were performed using an atomic force microscope (AFM) (Bruker Dimension Icon). Each group of fiber membranes was cut into 1.5×1.5 cm rectangles and coated with conductive aluminum tape on both sides to serve as electrodes. Copper wires were connected to the electrodes on opposite sides, and the entire assembly was sealed with polyimide (PI, DuPont) tape to form a piezoelectric sensor. The output electrical signal was measured directly using an electrometer (Keithley 6517) and an oscilloscope (HDO 6104). Considering the subsequent use of ultrasound as an external force stimulus, ultrasound waves with a frequency of 1 MHz were applied via an ultrasonic probe to induce the piezoelectric effect. The voltage output of each fiber membrane group was recorded, and the voltage output of the bilayer nanofiber scaffold was measured at different power densities. Using COMSOL Multiphysics software, theoretical simulations were conducted on the stress and potential distributions of PLLA and the bilayer nanofiber scaffold.

Additionally, the impact of degradation on scaffold performance was investigated. Specifically, samples (2 cm × 2 cm) were immersed in PBS-containing test tubes and placed in an incubator set at 37°C and 60 rpm for a 30-week degradation assessment. Changes in sample morphology and piezoelectric properties were simultaneously evaluated. To investigate the scaffold's fully degradable properties, we selected a 60°C oven to observe its degradation behavior and calculate mass loss.

5.4 | Cell Culture and Cell Viability

BMSCs were isolated from the cranial bone tissue of 7-day-old Sprague–Dawley rats and cultured and passaged in cell culture medium (α-MEM supplemented with 10% FBS and 1% PS). For differentiation, BMSCs were cultured in culture medium with tenogenic (100 μg/mL ascorbic acid), chondrogenic (1 mM sodium pyruvate, 10 ng/mL TGF-β3, 0.1 μM dexamethasone, 1% ITS cell culture supplement, 1 μM 2-Phospho-L-ascorbic acid), and osteogenic (50 μg/mL ascorbic acid, 10 μM dexamethasone, 2 mM β-glycerophosphate) supplements, respectively. Ultrasound stimulation (US, Chattanooga) was applied with the following parameters: the frequency was 1 MHz, the power was 0.5 W/cm^2, the duty cycle was 10%, duration was 2 min per day. The viability of BMSCs in different groups was assessed using a Cell Counting Kit-8 (CCK-8) assay. After culturing for 1, 3, and 5 days, the culture medium was replaced with 10% CCK-8 solution. Following an incubation period of 30 min at 37°C, the absorbance at a wavelength of 450 nm was measured using a microplate reader (Varioskan, Thermo Fisher Scientific Inc.).

5.5 | ALP Activity and Staining

To assess the activity and expression of ALP, BMSCs were cultured in osteogenic medium for 7 days. ALP activity was quantified by alkaline phosphatase assay kit according to the manufacturer's protocol, and the absorbance was measured at 405 nm ($n = 3$). For ALP staining, an alkaline phosphatase stain kit was applied according to the manufacturer's instructions, and the images were captured under a light microscope.

5.6 | ARS Staining and Alcian Blue Staining

To evaluate the potential for matrix mineralization during osteogenesis, BMSCs in different groups were cultured in osteogenic medium for 14 days. The BMSCs were fixed with 4% PFA for 15 min at room temperature. Subsequently, the fixed cells were stained with ARS solution for 20 min and then washed three times with PBS. Images were captured using a light microscope, and the mineralized area was quantified using ImageJ software. The accumulation of sulfated glycosaminoglycans (GAGs) was evaluated by Alcian blue staining. BMSCs were cultured in chondrogenic medium for 7 days. Following the culture period, cells were fixed with 4% PFA for 15 min at room temperature. They were then stained with Alcian blue solution for 15 min and washed three times with PBS. Images were obtained using an optical microscope.

5.7 | Immunofluorescent Staining Assay

To assess cell morphology and differentiation, immunofluorescence staining was performed. Briefly, BMSCs cultured on the scaffolds were fixed with 4% PFA for 15 min and then permeabilized with 0.3% Triton X-100 for 10 min. For the examination of the differentiation levels of BMSCs across different groups, cells were blocked with 5% goat serum for 45 min at room temperature. Subsequently, the samples were incubated overnight at 4°C with the following primary antibodies: anti-Collagen type I for tenogenesis, anti-SOX9 for chondrogenesis, and anti-RUNX2 for osteogenesis. After washing with PBS three times, the different groups were incubated with goat anti-rabbit IgG (H + L) secondary antibody (Alexa Fluor-488) at 37°C in the dark for 1 h. To visualize the actin cytoskeleton and cell morphology, the samples were stained with Phalloidin-iFluor 555 for 45 min at room temperature. Similar staining was performed on COL-X at the fiber interface. Finally, the cell nuclei were counterstained with DAPI. Images were acquired with a confocal fluorescence

microscope (CLSM, Leica SP8), and mean fluorescence intensity was quantified using ImageJ.

5.8 | Real-Time Quantitative PCR Assay

Total RNA was extracted using Trizol reagent. Briefly, cell samples were washed three times with PBS. Subsequently, cells were lysed in 200 μL of Trizol, and the lysate was transferred to an RNase-free microcentrifuge tube on ice. For phase separation, 40 μL of chloroform was added to the lysate. The mixture was vortexed vigorously, incubated at 4°C for 5 min, and then centrifuged at 12 000 rpm for 15 min at 4°C. The upper aqueous phase, containing the total RNA, was carefully collected and transferred to a new RNase-free tube. To precipitate the RNA, 100 μL of isopropanol was added to the aqueous phase. The solution was mixed thoroughly and incubated at 4°C for 15 min, followed by centrifugation at 12 000 rpm for 10 min at 4°C. After centrifugation, the supernatant was discarded, and the RNA was washed with 1 mL of 75% ethanol, followed by centrifugation at 12 000 rpm for 5 min at 4°C. The ethanol was carefully removed, and any residual ethanol was removed by centrifugation at 7500 rpm for 5 min and subsequent air-drying of the pellet. Finally, resuspended the RNA in 30 μL of RNase-free water.

The concentration and purity of the extracted RNA were determined by measuring the absorbance at 260 and 280 nm using a NanoDrop (Thermo Fisher). RNA samples with an A260/280 ratio between 1.6 and 2.0 were used for the subsequent experiment. Equal quantities of total RNA in each group were reverse transcribed to cDNA by HiScript II Q RT SuperMix according to the manufacturer's instructions. cDNA was amplified with Taq Pro Universal SYBR qPCR Master Mix and primer (synthesized by Tsingke biotechnology, sequences are listed in Table S1) on a real-time PCR detection system (QuantGene 9600, Bioer technology). The relative mRNA expression levels were calculated using the $2^{-\Delta\Delta Ct}$ method and normalized to the expression of the housekeeping gene (β-actin).

5.9 | Transcriptome Sequencing and Bioinformatic Analysis

Total RNA was extracted from the BMSCs culture on scaffolds with/without ultrasound stimulation using the previous methods. RNA sequencing ($n = 3$) was performed by Novogene Co., Ltd. Differential gene expression analysis between groups was performed using the DESeq2 R package. Genes with an adjusted p-value (p_{adj}) < 0.05 and an absolute log2 (fold change) > 0.5 were identified as differentially expressed genes (DEGs). Kyoto Encyclopedia of Genes and Genomes (KEGG) pathway enrichment analysis was performed using the clusterProfiler R package, with p-values < 0.05 considered significant. In parallel, Gene Set Enrichment Analysis (GSEA) was performed on the entire ranked gene list to identify enriched pathways. After cell lysis, the cells were centrifuged, and the protein concentration was determined. Subsequently, equal amounts of protein were separated by 10% SDS-polyacrylamide gel electrophoresis and then transferred to a polyvinylidene difluoride membrane. After being blocked in 5% non-fat milk for 1 h, the membranes were incubated overnight at 4°C with the following primary antibodies. Subsequently, the membranes were incubated with horseradish peroxidase-conjugated IgG, and protein bands were detected.

5.10 | Animal Model and Surgical Procedure

Eight-week-old male Sprague–Dawley (SD) rats were purchased from SPF Biotechnology Co., Ltd. The experimental protocol was designed according to the previously described RCT models [20]. All animal procedures were approved by the lab of Animal Experimental Ethical Inspection of Small Animal Experimental Platform of National Key Laboratory (NO. 2024014LZ). All animals were randomly divided into four groups: suture with/without US and scaffold with/without US ($n = 3$). Rats were anesthetized via isoflurane inhalation. After shaving the limb, a 2 cm longitudinal incision was made over the greater tuberosity of the humerus. The supraspinatus tendon was exposed through layer-by-layer dissection and then sharply transected at the footprint site. Subsequently, freshen the footprint and create two crisscrossing bone tunnels through the greater tuberosity using a 25-gauge needle. The residual tendon was then sutured to the footprint using the modified Mason–Allen method. The scaffold was then implanted between the tendon and bone and fixed with sutures. Finally, the incision was closed layer by layer. US was applied with the following parameters: the frequency was 1 MHz, the power was 0.5 W/cm^2, the duty cycle was 10%, the duration was 20 min per day, 4 days per week. Rats were sacrificed at weeks 4 and 8 post-surgery, and the tendon–humeral complexes were collected for the subsequent evaluation.

5.11 | Gait Analysis

Gait analysis was performed at 4 and 8 weeks post-surgery to evaluate functional recovery according to a previously reported method [60]. Briefly, the forelimbs of rats were stained with black ink. All animals were then walked along a narrow acrylic corridor lined with white paper, and the paw prints were collected for the stride length and step length evaluation.

5.12 | Micro-CT Analysis

The tendon–humeral complexes were scanned using a micro-CT system (PE Quantum GX, Perkin Elmer). The scanning parameters were as follows: FOV of 25 mm, voltage of 90 kV, current of 88 μA, and exposure time of 4 min. The raw data were reconstructed into 3D using CTvox 3.3 (Bruker), and the bone volume/tissue volume (BV/TV) was quantified using CTAn (Bruker).

5.13 | Biomechanical Analysis

The biomechanical properties of the regenerated tissue were evaluated at 4 and 8 weeks post-surgery using a universal testing machine (ESM301, Mark-10). Before testing, each tendon–humeral complex was carefully dissected to remove extraneous soft tissues. To enhance grip and prevent slippage, both the humeral shaft and the free muscle end of the supraspinatus were

first wrapped with medical gauze before being secured in the machine's clamps. The specimen was mounted on the machine, aligned with the longitudinal axis of the supraspinatus, and kept hydrated with PBS throughout the test. The load was applied at a constant displacement rate of 10 mm/min until complete failure. The ultimate failure load (N) was determined as the peak load, and stiffness (N/mm) was calculated from the slope of the linear region.

5.14 | Histological Analysis

The tendon–humeral complexes were fixed in 4% PFA for 48 h and subsequently decalcified in 12.5% ethylenediaminetetraacetic acid (EDTA) for 25 days. The decalcified samples were dehydrated through a graded ethanol, cleared in xylene, and embedded in paraffin wax. The paraffin blocks were then cut into 5 μm-thick slices. For histological evaluation, Hematoxylin and Eosin (H&E) staining was performed to evaluate the tissue morphology and cellularity. Masson's trichrome staining was used to assess collagen deposition and maturity at the healing interface. To visualize GAGs and cartilage formation, Safranin O/Fast Green staining was conducted. Additionally, Picrosirius red staining, when viewed under polarized light, was used to analyze the organization and maturity of collagen fibers. Tendon maturing score was used to evaluate the histological repair (see Table S2)

For immunohistochemistry (IHC), sections were first deparaffinized, rehydrated, and subjected to heat-induced antigen retrieval. The slices were incubated at 4°C overnight with anti-collagen type II. Subsequently, the slices were incubated with HRP-conjugated secondary antibody. Immunoreactivity was visualized using a diaminobenzidine (DAB) substrate kit, and the sections were counterstained with hematoxylin.

For immunofluorescence staining, the slices were incubated overnight at 4°C with primary antibodies as follows: OCN (1:200), COL2A1 (1:50), and α-SMA (1:200). Subsequently, the slices were incubated with secondary antibody and counterstained with DAPI.

5.15 | Statistical Analysis

All statistical analyses were performed using GraphPad Prism 8.0. All data are presented as the means ± standard error of the means (S.E.M.) from at least three independent experiments. A one-way analysis of variance (ANOVA) was performed to compare the differences between groups, followed by Tukey's post-hoc test for multiple comparisons. A p-value of less than 0.05 was considered statistically significant ($p < 0.05$).

Acknowledgements

This work is supported by the Beijing Natural Science Foundation (L245015, Z240022, and 25JL006 to Z. Li), the National Natural Science Foundation of China (T2125003 and U25A20417 to Z. Li), the National Natural Science Foundation of China (82272493 to Y. Zhao), and the Hunan Provincial Science Fund for Distinguished Young Scholars (2024JJ2089 to Y. Li).

Conflicts of Interest

The authors declare no conflicts of interest.

Data Availability Statement

The data that support the findings of this study are available from the corresponding author upon reasonable request.

References

1. L. Du, J. F. Wu, Y. H. Han, and C. T. Wu, "Immunomodulatory Multicellular Scaffolds for Tendon-to-Bone Regeneration," *Science Advances* 10 (2024): adk6610, https://doi.org/10.1126/sciadv.adk6610.

2. M. Y. Fu, Q. M. Han, X. L. Li, et al., "Vapor Welding-Assisted Electrospinning: Bioactive Composite Patch With Superior Mechanical Strength for Rotator Cuff Tears," *Advanced Engineering Materials* 27 (2025): 2500960, https://doi.org/10.1002/adem.202500960.

3. Y. W. Zhu, B. Y. Dai, S. Zhang, et al., "Tissue Mimetic Membranes for Healing Augmentation of Tendon–Bone Interface in Rotator Cuff Repair," *Advanced Materials* 37 (2025): 2407358.

4. R. H. Yang, G. Li, C. Y. Zhuang, et al., "Gradient Bimetallic Ion-Based Hydrogels for Tissue Microstructure Reconstruction of Tendon-to-Bone Insertion," *Science Advances* 7 (2021): abg3816.

5. M. R. Huang, W. Li, Y. Y. Sun, et al., "Janus Piezoelectric Adhesives Regulate Macrophage TRPV1/Ca2+/cAMP Axis to Stimulate Tendon-to-Bone Healing by Multi-Omics Analysis," *Bioactive Materials* 50 (2025): 134.

6. I. Kurtaliaj, E. D. Hoppe, Y. X. Huang, et al., "Python Tooth-Inspired Fixation Device for Enhanced Rotator Cuff Repair," *Science Advances* 10 (2024): adl5270, https://doi.org/10.1126/sciadv.adl5270.

7. J. J. Wang, J. C. Dai, D. J. Jiao, et al., "A Twin-Track Therapeutic Strategy for Massive Rotator Cuff Tears Based on Robust and Piezoelectric Nanocomposite Hydrogel Films," *Chemical Engineering Journal* 518 (2025): 164458, https://doi.org/10.1016/j.cej.2025.164458.

8. J. H. Yea, T. S. Bae, B. J. Kim, Y. W. Cho, and C. H. Jo, "Regeneration of the Rotator Cuff Tendon-to-Bone Interface Using Umbilical Cord-Derived Mesenchymal Stem Cells and Gradient Extracellular Matrix Scaffolds From Adipose Tissue in a Rat Model," *Acta Biomaterialia* 114 (2020): 104–116, https://doi.org/10.1016/j.actbio.2020.07.020.

9. X. X. Li, R. Y. Cheng, Z. Y. Sun, et al., "Flexible Bipolar Nanofibrous Membranes for Improving Gradient Microstructure in Tendon-to-Bone Healing," *Acta Biomaterialia* 61 (2017): 204–216, https://doi.org/10.1016/j.actbio.2017.07.044.

10. S. Tarafder, J. A. Brito, S. Minhas, L. Effiong, S. Thomopoulos, and C. H. Lee, "In Situ Tissue Engineering of the Tendon-to-Bone Interface by Endogenous Stem/Progenitor Cells," *Biofabrication* 12 (2020): 015008, https://doi.org/10.1088/1758-5090/ab48ca.

11. W. Su, J. S. Guo, J. J. Xu, et al., "Gradient Composite Film With Calcium Phosphate Silicate for Improved Tendon-to-Bone Intergration," *Chemical Engineering Journal* 404 (2021): 126473, https://doi.org/10.1016/j.cej.2020.126473.

12. X. P. Jiang, Y. F. Kong, M. Kuss, et al., "3D Bioprinting of Multilayered Scaffolds With Spatially Differentiated ADMSCs for Rotator Cuff Tendon-to-Bone Interface Regeneration," *Applied Materials Today* 27 (2022): 101510.

13. L. Fang, X. Q. Lin, R. Xu, et al., "Advances in the Development of Gradient Scaffolds Made of Nano-Micromaterials for Musculoskeletal Tissue Regeneration," *Nano-Micro Letters* 17 (2025): 75, https://doi.org/10.1007/s40820-024-01581-4.

14. M. J. Yuan, X. M. Dai, Y. X. Yang, et al., "An Injectable BMP-2-Releasing Porous Hydrogel Regulating the Paracrine Effects of ADSCs Promotes Tendon-to-Bone Healing in Rotator Cuff Repair," *Advanced Science* 12 (2025): 15923, https://doi.org/10.1002/advs.202415923.

15. T. Wu, X. Li, J. Xue, and Y. Xia, "Rational Fabrication of Functionally-Graded Surfaces for Biological and Biomedical Applications," *Accounts of Materials Research* 5 (2024): 1507–1519, https://doi.org/10.1021/accountsmr.4c00186.

16. W. Kim, D. R. Kwon, H. Lee, et al., "3D Bioprinted Multi-Layered Cell Constructs With Gradient Core-Shell Interface For Tendon-to-Bone Tissue Regeneration," *Bioactive Materials* 43 (2025): 471.

17. L. F. Li, R. N. Hao, J. J. Qin, et al., "Electrospun Fibers Control Drug Delivery for Tissue Regeneration and Cancer Therapy," *Advanced Fiber Materials* 4 (2022): 1375.

18. L. Li, X. Cui, R. Luo, and Z. Li, "Piezoelectric Electrospun Fibers for Tissue Regeneration: Synergizing Microarchitecture and Enhancement Strategies," *Science Bulletin* 71 (2026): 857–876, https://doi.org/10.1016/j.scib.2025.12.031.

19. M. Hao, Y. D. Chen, S. Thomopoulos, and Y. N. Xia, "Biomimetic Scaffolds With Dual Gradients of Biological Effectors for Tendon-to-Bone Repair," *Advanced Healthcare Materials* 14 (2025): 2503171, https://doi.org/10.1002/adhm.202503171.

20. S. Chae, U. Yong, W. Park, et al., "3D Cell-Printing of Gradient Multi-Tissue Interfaces for Rotator Cuff Regeneration," *Bioactive Materials* 19 (2023): 611–625.

21. Y. Z. Sun, R. W. Sheng, Z. C. Cao, et al., "Bioactive Fiber-Reinforced Hydrogel to Tailor Cell Microenvironment for Structural and Functional Regeneration of Myotendinous Junction," *Science Advances* 10 (2024): adm7164, https://doi.org/10.1126/sciadv.adm7164.

22. T. Y. Lei, T. Zhang, T. S. Fang, et al., "Engineering a Stem Cell-Embedded Bilayer Hydrogel with Biomimetic Collagen Mineralization for Tendon-Bone Interface Healing," *Bioactive Materials* 49 (2025): 207.

23. Z. C. Ding, Y. R. Cai, H. C. Sun, et al., "Janus Hydrogel Microrobots With Bioactive Ions for the Regeneration of Tendon-Bone Interface," *Nature Communications* 16 (2025): 2189, https://doi.org/10.1038/s41467-025-57499-x.

24. J. S. Jiang, J. P. Wan, X. Y. Yu, et al., "Biomimetic Patch With Gradient-Induced Regeneration for Tendon-Bone Interface to Repair Rotator Cuff Injury," *Chemical Engineering Journal* 506 (2025): 159985, https://doi.org/10.1016/j.cej.2025.159985.

25. W. Song, Y. Guo, W. C. Liu, et al., "Circadian Rhythm-Regulated ADSC-Derived sEVs and a Triphasic Microneedle Delivery System to Enhance Tendon-to-Bone Healing," *Advanced Materials* 36 (2024): 2408255, https://doi.org/10.1002/adma.202408255.

26. Q. T. Ehlen, J. P. Costello, N. A. Mirsky, et al., "Treatment of Bone Defects and Nonunion Via Novel Delivery Mechanisms, Growth Factors, and Stem Cells: A Review," *ACS Biomaterials Science & Engineering* 10 (2024): 7314–7336, https://doi.org/10.1021/acsbiomaterials.4c01279.

27. N. Saveh-Shemshaki, M. A. Barajaa, T. Otsuka, E. S. Mirdamadi, L. S. Nair, and C. T. Laurencin, "Electroconductivity, a Regenerative Engineering Approach to Reverse Rotator Cuff Muscle Degeneration," *Regenerative Biomaterials* 10 (2023): rbad099, https://doi.org/10.1093/rb/rbad099.

28. X. F. Li, Y. B. Liu, Q. N. Yang, et al., "Injectable Piezoelectric Hydrogel Promotes Tendon–Bone Healing Via Reshaping the Electrophysiological Microenvironment and M2 Macrophage Polarization," *ACS Applied Materials & Interfaces* 17 (2025): 22210–22231, https://doi.org/10.1021/acsami.4c21011.

29. W. Li, Y. T. Mo, S. H. Xie, et al., "Self-Reinforced Piezoelectric Chip for Scaffold-Free Repair of Critical-Sized Bone Defects," *Nature Communications* 16 (2025): 5800, https://doi.org/10.1038/s41467-025-61243-w.

30. J. W. Yang, L. F. Li, Y. R. Hu, Z. Li, and W. Hua, "Novel Electroactive Therapeutic Platforms for Cardiac Arrhythmia Management," *Advanced Science* 12 (2025): 2500061, https://doi.org/10.1002/advs.202500061.

31. Q. Zhang, J. H. Zhu, X. Fei, and M. F. Zhu, "A Janus Nanofibrous Scaffold Integrated With Exercise-Driven Electrical Stimulation and Nanotopological Effect Enabling the Promotion of Tendon-to-Bone Healing," *Nano Today* 55 (2024): 102208, https://doi.org/10.1016/j.nantod.2024.102208.

32. Y. Bai, H. Meng, Z. Li, and Z. L. Wang, "Degradable Piezoelectric Biomaterials for Medical Applications," *MedMat* 1 (2024): 40–49, https://doi.org/10.1097/mm9.0000000000000002.

33. Y. Shan, L. Xu, X. Cui, et al., "A Neurodevelopment-Inspired Self-Evolving Scaffold for Nerve Regeneration," *Cell Biomaterials* 1 (2025): 100006.

34. E. Wang, M. Wu, L. Luo, et al., "Symbiotic Biodegradable Flexible Supercapacitor In Vivo," *Device* 3 (2025): 100724.

35. F. A. Azaman, F. Daubiné, A. Lebatard, M. E. Brennan Fournet, and D. M. Devine, "Chitosan/Hydroxyapatite Scaffolds With P28 as a Promising Osteoinductive Scaffold for Bone Healing Applications," *Micro* 3 (2023): 118–142, https://doi.org/10.3390/micro3010010.

36. R. Z. Luo, Y. J. Xiong, J. X. Li, et al., "Piezoelectric Injectable Anti-Adhesive Hydrogel to Promote Endogenous Healing of Tendon Injuries," *Advanced Materials* 37 (2025): 2501306, https://doi.org/10.1002/adma.202501306.

37. T. Vinikoor, G. K. Dzidotor, T. T. Le, et al., "Injectable and Biodegradable Piezoelectric Hydrogel for Osteoarthritis Treatment," *Nature Communications* 14 (2023): 6257, https://doi.org/10.1038/s41467-023-41594-y.

38. D. Yu, L. Li, X. Cui, et al., "Synergistic Piezoelectricity and Lubrication in an Injectable Hydrogel for Osteochondral Regeneration," *Advanced Functional Materials* 36 (2026): 75561, https://doi.org/10.1002/adfm.75561.

39. X. Cui, L. Xu, Y. Shan, et al., "Piezocatalytically-Induced Controllable Mineralization Scaffold With Bone-Like Microenvironment to Achieve Endogenous Bone Regeneration," *Science Bulletin* 69 (2024): 1895–1908, https://doi.org/10.1016/j.scib.2024.04.002.

40. Y. Xiong, R. Luo, Y. Qi, et al., "Flexible Stretchable Piezoelectric Films for Tissue Repair and Health Detection," *Small Methods* 9 (2025): 00247, https://doi.org/10.1002/smtd.202500247.

41. L. Li, J. Yang, Y. Wang, et al., "Topologically Structured PLLA Fibers With Stress Concentration Effects for Health Monitoring," *Advanced Science* 13 (2026): 75619, https://doi.org/10.1002/advs.75619.

42. K. Zhang, Y. Fan, N. Dunne, and X. Li, "Effect of Microporosity on Scaffolds for Bone Tissue Engineering," *Regenerative Biomaterials* 5 (2018): 115–124, https://doi.org/10.1093/rb/rby001.

43. Z. Yin, X. Chen, J. L. Chen, et al., "The Regulation of Tendon Stem Cell Differentiation by the Alignment of Nanofibers," *Biomaterials* 31 (2010): 2163–2175, https://doi.org/10.1016/j.biomaterials.2009.11.083.

44. Q. Jiang, L. Wang, Z. Liu, et al., "Canine ACL Reconstruction with an Injectable Hydroxyapatite/Collagen Paste for Accelerated Healing of Tendon-Bone Interface," *Bioactive Materials* 20 (2023): 1.

45. J. Chen, Q.-Y. Zhang, J. Tan, et al., "Enhanced Fibrocartilage Regeneration at the Tendon-Bone Interface Injury Through Extracellular Matrix Hydrogel Laden With bFGF-Overexpressing Human Urine-Derived Stem Cells," *Chemical Engineering Journal* 497 (2024): 154333, https://doi.org/10.1016/j.cej.2024.154333.

46. G.-P. Dang, W. Qin, Q.-Q. Wan, et al., "Regulation and Reconstruction of Cell Phenotype Gradients Along the Tendon-Bone Interface," *Advanced Functional Materials* 33 (2023): 2210275, https://doi.org/10.1002/adfm.202210275.

47. F. You, X. Chen, D. M. L. Cooper, T. Chang, and B. F. Eames, "Homogeneous Hydroxyapatite/Alginate Composite Hydrogel Promotes Calcified Cartilage Matrix Deposition With Potential for Three-Dimensional Bioprinting," *Biofabrication* 11 (2019): 015015, https://doi.org/10.1088/1758-5090/aaf44a.

48. B. Xie, H. Ma, F. Yang, et al., "Development and Evaluation of 3D Composite Scaffolds With Piezoelectricity and Biofactor Synergy for Enhanced Articular Cartilage Regeneration," *Journal of Materials Chemistry B* 12 (2024): 10416–10433, https://doi.org/10.1039/D4TB01319K.

49. K. Li, W. Xu, Y. Chen, et al., "Piezoelectric Nanostructured Surface for Ultrasound-Driven Immunoregulation to Rescue Titanium Implant Infection," *Advanced Functional Materials* 33 (2023): 2214522, https://doi.org/10.1002/adfm.202214522.

50. Y. Wang, Y. Wang, X. Wang, et al., "Biodegradable and Electroactive Cryogel Microspheres for Neurovascularized Bone Regeneration," *Matter* 8 (2025): 102366.

51. J. S. L. Yu and W. Cui, "Proliferation, Survival and Metabolism: The Role of PI3K/AKT/mTOR Signalling in Pluripotency and Cell Fate Determination," *Development* 143 (2016): 3050–3060.

52. C. Chen, X. Zheng, C. Wang, et al., "CTHRC1 Attenuates Tendinopathy Via Enhancing EGFR/MAPK Signaling Pathway," *Advanced Science* 11 (2024): 2406611, https://doi.org/10.1002/advs.202406611.

53. V. Russo, G. Prencipe, A. Mauro, et al., "Assessing the Functional Potential of Conditioned Media Derived From Amniotic Epithelial Stem Cells Engineered on 3D Biomimetic Scaffolds: An In Vitro Model for Tendon Regeneration," *Materials Today Bio* 25 (2024): 101001, https://doi.org/10.1016/j.mtbio.2024.101001.

54. N. Liu, D. Fu, J. Yang, et al., "Asiatic Acid Attenuates Hypertrophic and Fibrotic Differentiation of Articular Chondrocytes Via AMPK/PI3K/AKT Signaling Pathway," *Arthritis Research & Therapy* 22 (2020): 112, https://doi.org/10.1186/s13075-020-02193-0.

55. T. Chen, Y. Peng, W. Hu, et al., "Irisin Enhances Chondrogenic Differentiation of Human Mesenchymal Stem Cells Via Rap1/PI3K/AKT Axis," *Stem Cell Research & Therapy* 13 (2022): 392, https://doi.org/10.1186/s13287-022-03092-8.

56. A. Vortkamp, K. Lee, B. Lanske, G. V. Segre, H. M. Kronenberg, and C. J. Tabin, "Regulation of Rate of Cartilage Differentiation by Indian Hedgehog and PTH-Related Protein," *Science* 273 (1996): 613–622, https://doi.org/10.1126/science.273.5275.613.

57. L. Li, A. Li, L. Zhu, L. Gan, and L. Zuo, "Roxadustat Promotes Osteoblast Differentiation and Prevents Estrogen Deficiency-Induced Bone Loss by Stabilizing HIF-1α and Activating the Wnt/β-Catenin Signaling Pathway," *Journal of Orthopaedic Surgery and Research* 17 (2022): 286, https://doi.org/10.1186/s13018-022-03162-w.

58. S. Yu, J. Du, Q. Zhang, Z. Li, S. Ge, and B. Ma, "Mitochondria-Targeted Polyphenol-Cysteine Nanoparticles Regulating AMPK-Mediated Mitochondrial Homeostasis for Enhanced Bone Regeneration," *Advanced Functional Materials* 34 (2024): 2402463, https://doi.org/10.1002/adfm.202402463.

59. Y. F. Yin, P. R. Zhao, X. Y. Xu, et al., "Piezoelectric Analgesia Blocks Cancer-Induced Bone Pain," *Advanced Materials* 36 (2024): 2403979, https://doi.org/10.1002/adma.202403979.

60. S.-Y. Chan, C.-W. Kuo, T.-T. Liao, C.-W. Peng, T.-H. Hsieh, and M.-Y. Chang, "Time-Course Gait Pattern Analysis in a Rat Model of Foot Drop Induced by Ventral Root Avulsion Injury," *Frontiers in Human Neuroscience* 16 (2022): 972316, https://doi.org/10.3389/fnhum.2022.972316.

Supporting Information

Additional supporting information can be found online in the Supporting Information section.

Supporting File: adma74137-sup-0001-SuppMat.docx.